1-1-2012

Laser Synthesis of Nanostructured Glass for Selective Cell Proliferation or Apoptosis

Champika Samarasekera
Ryerson University

LASER SYNTHESIS OF NANOSTRUCTURED GLASS FOR SELECTIVE CELL PROLIFERATION OR APOPTOSIS

By

Champika Samarasekera, B.Sc. (Honours)
Physics
Dalhousie University, 2003

A thesis

presented to Ryerson University

in partial fulfillment of the

requirements for the degree of

Master of Applied Science

in the Program of

Aerospace Engineering

Toronto, Ontario, Canada, 2012

Author's Declaration

I hereby declare that I am the sole author of this thesis. This is a true copy of the thesis, including any required final revisions, as accepted by my examiners.

I authorize Ryerson University to lend this thesis to other institutions or individuals for the purpose of scholarly research

I further authorize Ryerson University to reproduce this thesis by photocopying or by other means, in total or in part, at the request of other institutions or individuals for the purpose of scholarly research.

I understand that my thesis may be made electronically available to the public.

Abstract

Laser Synthesis of Nanostructured Glass for Selective Cell Proliferation or Apoptosis

Champika Samarasekera, Master of Applied Science, Aerospace Engineering, Ryerson University, Toronto, 2012

The state-of-the-art in synthesis of nanostructured cell and contra-cell surfaces relies on techniques that utilize elaborate precursor chemicals, catalysts, or vacuum conditions, and any combination thereof. Two types of nanostructures, Na_2O nanotips and SiO_2 nanofibers, have been fabricated on soda-lime glass using ultrafast laser ablation. Control over nanotip width was demonstrated via laser dwell time and a new tip formation mechanism is proposed. The nanofibers generated in this work display a level of nanomorphology unseen in other fiber fabrication methods. The resulting fibers show striking morphological similarity to proteins that comprise the natural extra cellular matrix. The interaction of both nanostructures with NIH 3T3 fibroblasts was explored by incubating nanostructured glass with fibroblasts over periods of 12 hours, 1 day, or 1 week. Nanotip structures appeared to induce apoptosis in cells while nanofibers influenced cells to display unique, healthy characteristics such as preferential adhesion to nanofibers and increased microvilli generation.

Acknowledgements

I would like to thank my supervisor Dr. Bo Tan for giving me this incredible opportunity and then sharing her knowledge in the realm of ultrafast laser ablation and nanofabrication. Her belief in my abilities, patience with my questions, and always insightful feedback were crucial to the completion of this thesis and my development as a scientist.

I would also like to thank Dr. Krishnan Venkatakrishnan for his constant support that came in the form of experimental guidance, timely observations and helpful advice. His mantra of judicious attention to detail while not losing sight of the big picture was relied upon by me time and again.

To my fellow partners in crime (lab members), thank you for letting me test my ideas, vent my frustrations, and share some laughs with you.

Most importantly, I would like to thank my incredible parents and wonderful sister who supported me when I couldn't, believed in me when I wouldn't, and motivated me when I didn't.

Finally, I'd like to thank Bodhi, for never complaining about the late hours and erratic schedules.

Table of Contents

Table of Figures

Nomenclature

1D	one dimensional
2D	two dimensional
3D	three dimensional
aECM	artificial extracellular matrix
α	absorption coefficient
c	speed of light in vacuum (2.998×10^{8} m·s^{-1})
D	diameter of laser beam incident on focusing lens
d_0	laser spot diameter
d_{min}	minimum laser spot diameter
ECM	extracellular matrix
EDX	energy dispersive X-ray
E	energy
f	pulse frequency
FBS	fetal bovine serum
h	Planck's constant (6.626x10-^{34} J·s)
k	extinction coefficient
λ	wavelength
l	focal length of lens
P	laser power
SCFH	standard cubic feet per hour
SEM	scanning electron microscope
τ_p	duration of laser pulse
TEM	transmission electron microscope

UV	ultraviolet
z	distance from laser focal point (also direction of laser propagation)

1. Introduction

1.1 Nanotechnology and Aerospace

The idea of manipulating individual atoms and molecules is certainly not a new one. Addressing members at a year-end American Physical Society meeting in 1959, the noted physicist Richard Feynman predicted the exciting possibilities and potential difficulties of controlling things on such a small scale [1]. Nearly two decades later Norio Taniguchi dubbed the mastery over materials at the molecular and atomic level "nanotechnology" [2]. Today, the term has been appropriated by society to describe science and engineering directed on the scale of 1 to 100 nanometers.

Structures at the nanometer scale are no longer governed by classical forces. In this regime quantum effects rule, and as a consequence, the material properties of so-called nanostructures become size-dependent. Furthermore, as a material's size decreases, the ratio of its surface area to volume increases; materials interact with the environment via their surfaces, thus larger surface areas result in materials with higher reactivity.

Interest in nanotechnology spans across many industries and there has been an influx of nanotechnology publications with potential applications in every regime of the aerospace sector. From nanocomposites with material properties that promise unheard of strength to weight ratios [3] for advanced aerospace structures, nanotextured materials that naturally repel dust, dirt, and water [4] for use on photovoltaic panels and windows, to more efficient propellants via nanocatalysts [5]. Many applications abound for a single nanomaterial or family of nanostructures and this has led to a curious confluence of nanotechnology, aerospace, and biology.

1.2 Nano, Aero, Bio?

With its many millennia of experience, nature has learned to exploit nanostructures to meet various functional requirements. The protection afforded by the internetworked mineral nanoplatelets that compose the scales of the *Arapaima gigas* fish allow it to thrive in piranha infested waters of the Amazon basin [6]. Ivory tusks are low thermal conductivity, high strength nanocomposite biominerals [7] that elephants use for foraging, digging and protection against predators. Even biological processes occur at the nanoscale; a single strand of DNA, one of the macromolecules essential for life, is less than 3 nm in width [8], and to transport oxygen from the lungs to other tissues and carry carbon dioxide back, the body relies on hemoglobin, a protein less than 6 nm in diameter [9].

Therefore, the potential exists for using synthetic nano-engineered materials to monitor or manipulate biological systems. The importance of this should not be overlooked, especially with regard to the mission critical requirements of human spaceflight and space habitation. The limited cargo capacity and access to resources while in space necessitates self-sufficiency. Thus, high-performance materials that can screen, maintain, and repair the health of astronauts would be of great utility. For example, in detecting biochemical damage or changes in cells from exposure to radiation or infectious agents that can impact astronaut health; in tight enclosed spaces where naturally antibacterial surfaces might help limit the spread of germs and disease; in gauze or wound dressings that could enhance the growth of cells and speed the recovery of injured astronauts reducing mission downtime. The inspiration to meet these needs can be drawn from the natural world.

1.3 *In vitro* and *in vivo:* Bridging the gap

In biomedicine, materials must meet some stringent criteria and foremost among them is the ability of a material to do no harm to surrounding tissue. A material usually achieves this by various degrees of chemical and biological inertness [10]. The efficacy of a biomedical device is higher when the possibility of host rejection is lowered; this can be accomplished if the material incorporates itself into the tissues that surround it, a trait defined as bioactivity [11]. Alongside the seemingly cross purposed requirements of inertness and bioactivity, some biomedical applications can benefit from material biodegradability. The obvious advantages to degrading implants are that removal becomes unnecessary and post-treatment care can be simplified.

As the term *in vitro* (Latin: in glass) would suggest, the traditional material for growing cells outside the body has been smooth glass surfaces. Of these, certain expensive varieties known as bioactive glasses are renowned for their biocompatibility with soft and hard tissues making them viable implant materials [12,13]. However, cells *in vivo* (Latin: within the living) grow on naturally occurring fibrillar structures known as the extracellular matrix (ECM). The ECM is not a single monolithic entity, but rather, a catchall term that describes a wide variety of structures that are tailored in shape, size, and consistency by and for the types of cells that use it.

1.3.1 The nanomaterials of the natural cell environment

Despite the wide variety of naturally occurring ECM structures, their inherent nanoscale dimensions are a commonality. The materials that primarily compose ECM structures are proteins such as laminin, fibronectin, elastin, and collagen.

1.3.1.1 Collagen

Being the most abundant protein in mammals, 20 types of collagens are known to exist and are secreted by many types of cells. Five of these collagen types can form fibrils found in

ECM tissues. The fibers are formed when collagen monomers align such that molecules from one row are staggered relative to the next. This arrangement appears on fibers as a periodic band 64-70 nm in width. The fibers themselves are typically 10-300 nm in diameter, hundreds of microns long and individual fibrils tend to braid into larger microscale diameter fibers [14]. In certain types of ECM tissues the collagen molecules form interlinked, complex, 3D arrays [14]. The collagen fibers help prevent tear damage to ECM tissue but elasticity is also required to allow tissues to stretch and recoil, a role played by another protein.

1.3.1.2 Elastin

Like collagen, elastin is a protein that is secreted by several cell types. It is believed that individual elastin molecules are randomly coiled and covalently bound to each other; the resulting cross-linked network gives the micron sized elastin fibers their extensibility [14].

1.3.1.3 Fibronectin and laminin

Binding cells to the majority of ECM tissues are short fibronectin fibrils about tens of nm in diameter, on the order of a 100 nm in length, and form fibrillar arrays [14,15]. One special case where an ECM is composed of a particular type of collagen requires laminin proteins for cell adhesion. The laminin molecules appear cross shaped with three short arms of approximately 50 nm and a longer arm twice that length [14]. Laminin tends to bind to laminin via the short arms allowing the molecules to form sheets and freeing the longer arm for cell attachment.

1.3.2 The nanostructure of the natural cell environment

All of the aforementioned proteins combine to form the crucial architecture of different ECM structures that are unique to particular cell or tissue types (see Figure 1-1 for examples). Subsequently, the ECM influences not only cell growth but also cell function [16,17]. The three

dimensional (3D) networked morphology of nanofibrous ECM tissues are hardly reflected in today's featureless, two dimensional (2D) conventional glass substrates.

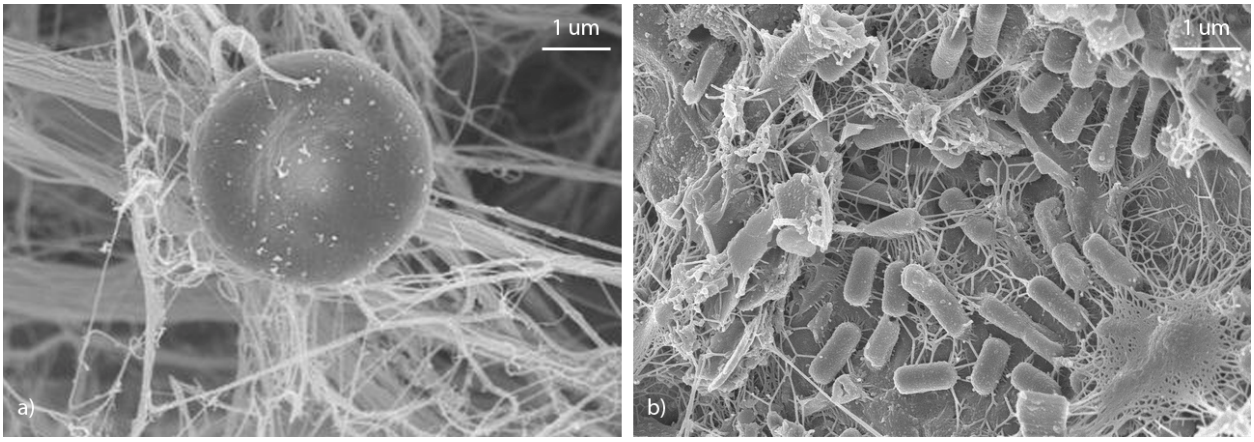

Figure 1-1 SEM micrographs of ECM produced by: **a)** mouse cremaster tissue with red blood cell [Image credit- Institute of Optics at University of Rochester, image created by Amir Prizant and Brian McIntyre]; **b)** bacterial microbes on a grain of sand [Image credit- Lewis Lab at Northeastern University, image created by Anthony D'Onforio, William H. Fowle, Eric J. Stewart and Kim Lewis].

Thus, synthetic materials that can mimic the intricate fibrillar architecture of the ECM are alluring options for potential cell growth substrates. Despite the wide variety of naturally occurring ECM structures, their inherent nanoscale dimensions are a commonality. To this end, researchers have explored creating artificial ECM (aECM) structures from nanofibers of various materials; typically this has required processing techniques such as electrospinning, laser spinning, self-assembly, or phase separation.

1.3.3 Electrospinning

The electrospinning technique is the most common fiber synthesis method and can generate fibers with diameters as large as a few micrometers and as small as tens of nanometers [18]. The procedure requires high voltage (typically 1 to 30 kV) to create a liquid jet by pushing a viscous liquid through a charged metal needle; a grounded collector plate is placed a short distance (typically 10 to 20 cm) below the needle [19]. As a droplet forms on the needle it

becomes charged and two types of electrostatic forces act on the droplet. First, the surface charges cause electrostatic repulsion; next, the external electric field exerts a Coulombic force. These forces shape the droplet into a feature known as a Taylor cone. The jet forms when the charged liquid overcomes its own surface tension. The liquid jet continues to stretch as it begins to evaporate into a fiber and, in what is called the instability region, the surface charges on the fiber interact with the external electric field causing the fiber to bend and whip rapidly. The collector plate attracts the fiber as it is deposited in a randomly oriented mat. A schematic of a typical electrospinning setup is shown in Figure 1-2.

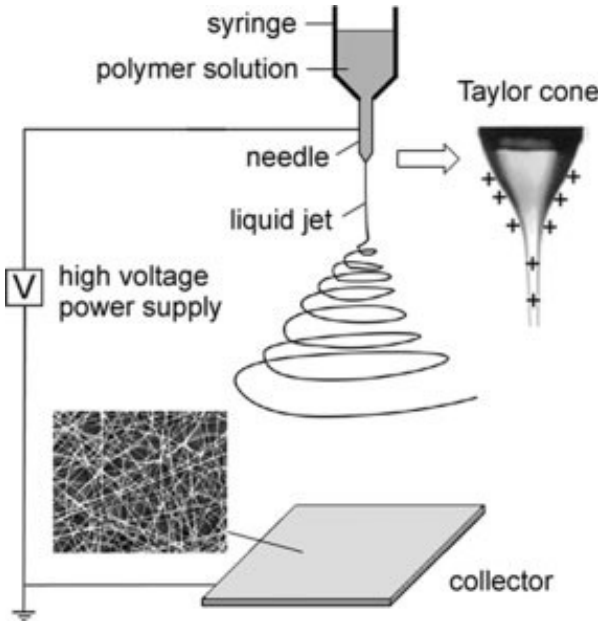

Figure 1-2 Schematic of conventional electrospinning setup with insets showing Taylor cone and typical SEM image of a nanofiber mat [19].

If the viscosity of the solution is too low it can complicate the electrospinning process by creating instabilities that tend to break the jet resulting in beads or spheres to form on the fibers. As can be seen in Figure 1-3, increasing the polymer concentration has been shown to decrease these irregularities but increase the diameter of the fibers [19,20].

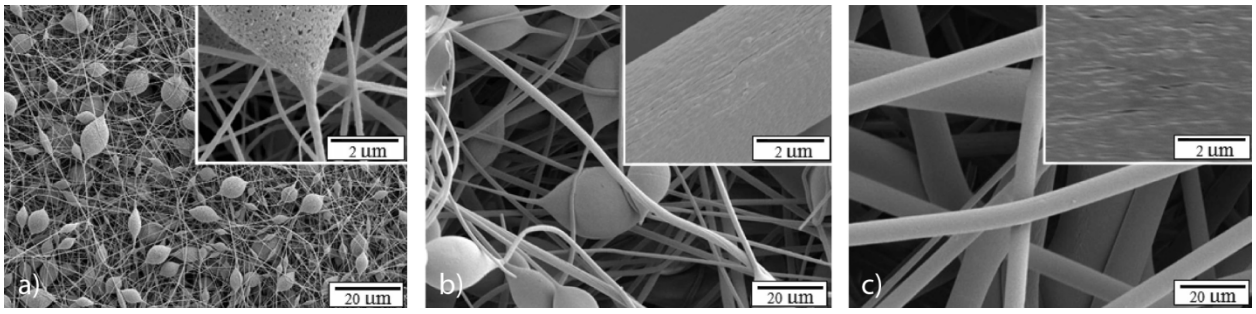

Figure 1-3 SEM micrographs of electrospun polystyrene fibers at **a)** 10 wt %; **b)** 20 wt %; **c)** 30 wt % with insets showing higher magnification detail of individual fibers, *Images modified from* [20].

The well-defined viscoelastic solutions required for electrospinning typically restricted researchers to using organic polymers. However, it has been demonstrated that composite fibers can be produced through the use of conventional precursor solutions that gradually evolve into a gel (sol-gel) [21]. In such cases, to retain the viscoelastic behavior common to organic polymer solutions, researchers fine tune pH value or aging conditions and thus control the rate of degradation in water (hydrolysis) of the sol-gel precursors.

This very method has also been attempted for forming nanofibrous glass. Since liquid glass (melt) is too viscous to be electrospun it is usually distributed in a polymer solution. After the polymer-melt is spun, further post-processing steps are required to amalgamate the glass fibers and remove the polymer precursors. The fibers can also be bundled and compacted to create much larger scale 3D structures as shown in Figure 1-4a [22]. Recently, a glassy boron oxide (B_2O_3) mixture was electrospun without the use of polymers [23]. However, the resulting fibers tend to be non-branching, single strands and thus morphologically dissimilar to ECMs (see Figure 1-4b). Furthermore, unlike true borosilicate glasses that contain elements like silicon, their suitability as structures for cell growth remains to be determined.

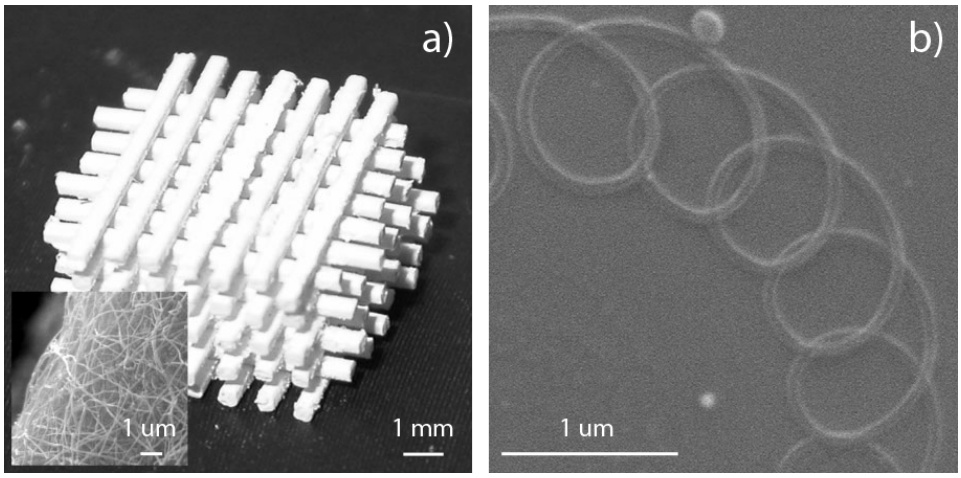

Figure 1-4 Electrospun glass fibers: **a)** from polymer-melt synthesis molded into macroscale structures with inset showing SEM micrograph of nanofiber structures at high magnification, *Image modified from* [22]; **b)** from melt-only synthesis, *Image modified from* [23].

The careful selection of polymer precursors required for maintaining an electrospinnable viscosity, the post processing routines required to remove these very same precursors, jet instability, and the lack of suitably crosslinked fiber strands have thus far limited electrospinning as a method for generating glass fibers for use as aECMs.

1.3.4 Laser spinning

This relatively recent technique (illustrated in Figure 1-5a) evolved from attempts to get cleaner and more efficient cuts in ceramics from a laser cutting set up [24]. Instead, Quintero et al discovered that nanowires were produced and deposited on the ceramic substrate. A high powered laser is focused on to a small volume of precursor material to quickly heat and then melt at very high temperatures. During this process inert gas is directed toward the melt at supersonic velocity to blow the molten material into a filament [24-26]. By constantly feeding precursor material in the path of the focused laser beam a continuous molten stream can be produced, combined with the rapid stretching and cooling action of the fast flowing gas, dense mats of intertwined nanofibers can be formed quite quickly. Typical fibers produced by laser

spinning range in diameter from several micrometers down to tens of nanometers while having lengths in the hundreds of micrometers (see Figure 1-5b).

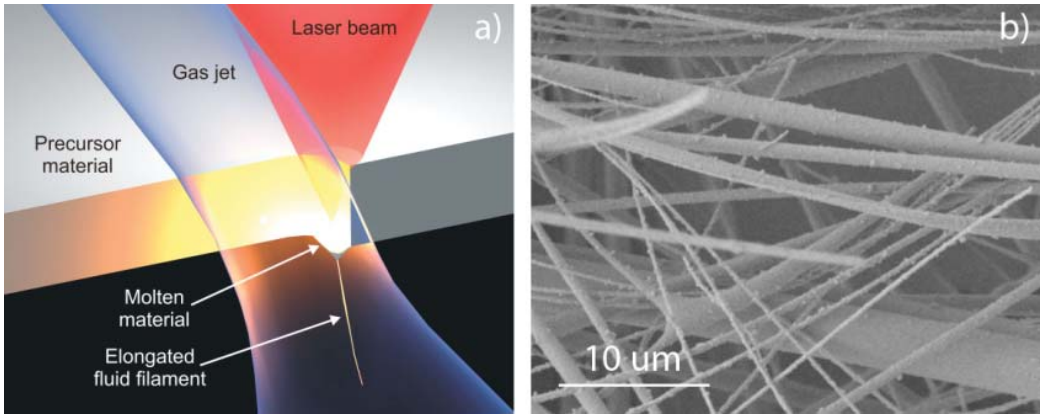

Figure 1-5 a) Illustration of the laser spinning process [26]; **b)** SEM micrograph showing the typical appearance of laser spun fibers, *Image modified from* [25].

Fibers have successfully been produced from various starting materials such as polycrystalline ceramics, soda-lime glass, and bioactive glass [24-26]. The rapid cooling of melted glass fiber by the fast flowing gas results in an amorphous rather than crystalline product that is very similar in composition to the bulk precursor material. The fibers produced during the laser spinning process break when surface tension causes instabilities in the elongated fluid filament before the fiber can solidify. Furthermore, due to geometric restrictions of the gas jet, drops of molten material larger than a few microns in diameter cannot elongate into nanofibers [24].

1.3.5 Self-assembly

A so-called 'bottom-up' approach, self-assembly is defined as a process by which pre-existing, individual components organize autonomously into structures absent human involvement [27]. The final shapes of the structures depend on the molecules used as building blocks and the weakly covalent or non-covalent forces between them. As the process requires

movement of components, self-assembly is ordinarily conducted in fluids. To build fibrous structures researchers used conically shaped molecules that aggregate concentrically and extend normal to the plane as seen in Figure 1-6 [28].

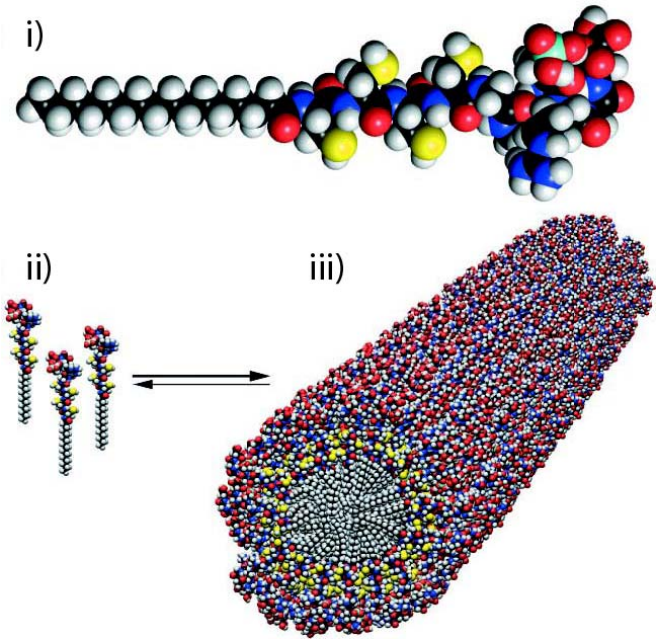

Figure 1-6 Illustration of self-assembly process: **i)** specially designed conically shaped molecule; **ii)** many molecules dispersed in solution; **iii)** weak and non-covalent forces cause molecules to attach in concentric fashion creating a nanofiber, *Image modified from* [28].

The resulting fibers are exceptionally small with diameters under 10 nm and form in parallel arrays (see Figure 1-7a). In order to replicate the cross-linking found in ECM structures the fibers are reoriented by the formation of covalent bonds via oxidation, a process known as 'covalent capture' (see Figure 1-7b).

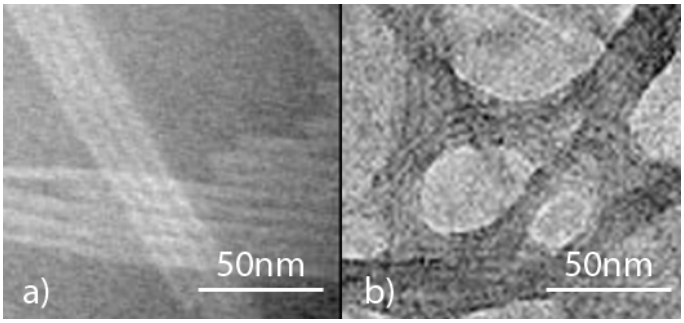

Figure 1-7 SEM micrographs of self-assembled nanofibers **a)** forming as ribbon-like parallel arrays; **b)** cross-linking after covalent capture, *Image modified from* [28].

The fundamental drawback to the self-assembly method is that the morphology of the final structure must be encoded in the smaller component parts. This requires intense management and planning in formulating the complex chemistries involved. Furthermore, the user is disadvantaged by the long processing times and post-processing steps necessary for elaborate structure formation.

1.3.6 Phase-separation

This multi-step process can produce polymer fibers with sizes between 50 to 500 nm [29,30]. First, a homogenous solution of polymer in solvent at a desired concentration is created. Second, the polymer solution is refrigerated or frozen to gelation temperature. Third, solvent exchange is facilitated via gel immersion in distilled water. Fourth, the gel is removed from the water, blotted dry and frozen. Finally, the frozen gel is lyophilized leaving behind a dried porous nanofibrous matrix (see Figure 1-8).

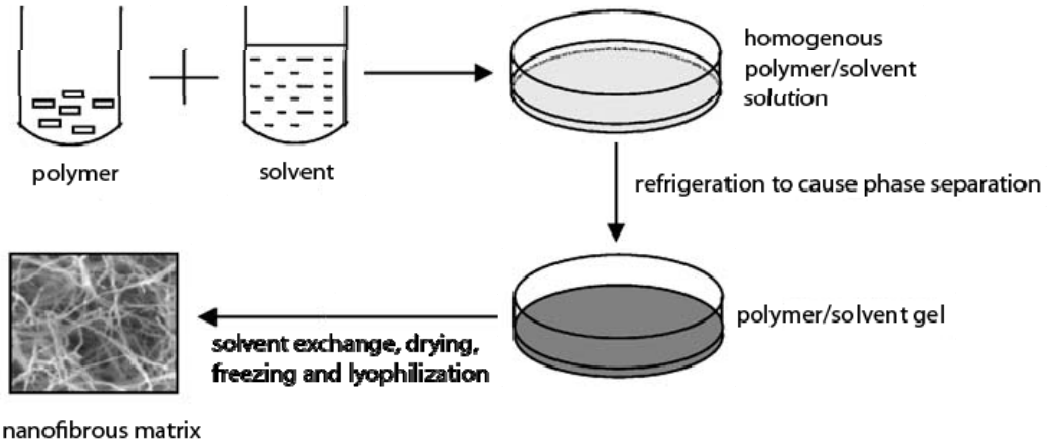

Figure 1-8 Schematic of phase-separation process for formation of nanofibrous scaffolds, *Image modified from* [30].

Depending on the type of polymer used, the fiber diameter and thus the porosity of the scaffolds can be dependent on polymer concentration (see Figure 1-9a-c) [29,30].

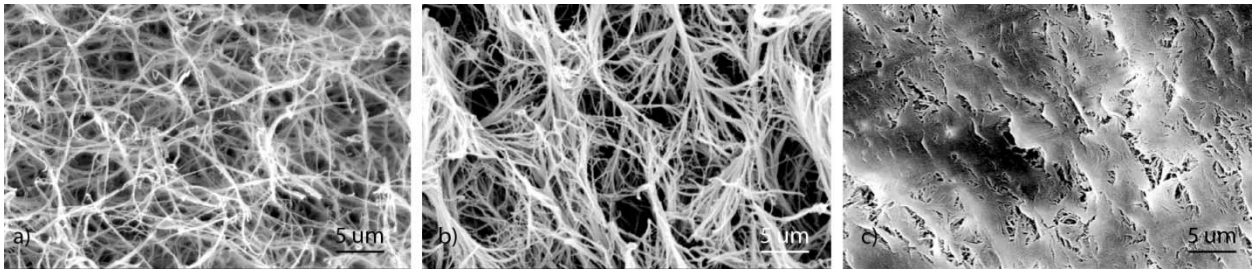

Figure 1-9 SEM micrographs of phase-separation processed nanofibrous scaffolds at varying concentrations of polymer **a)** 2% wt/v; **b)** 5% wt/v; **c)** 9% wt/v, *Images modified from* [30].

Additionally, gelation temperature can influence the production of non-fibrous structures (see Figure 1-10a-c) [29].

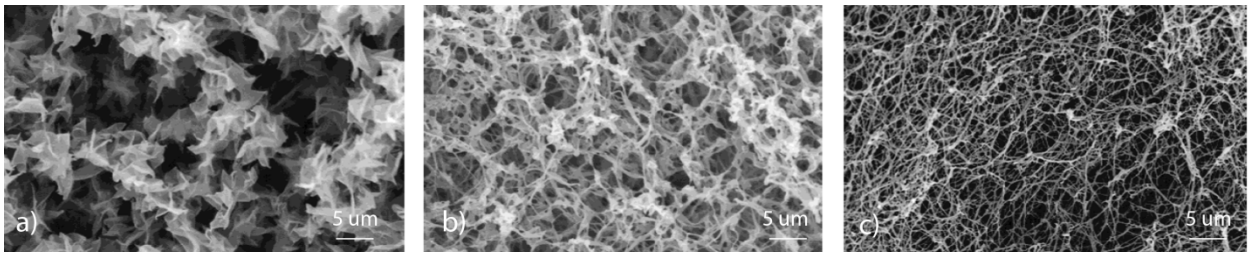

Figure 1-10 SEM micrographs of phase-separation processed scaffolds showing variations in morphology from platelets to nanofibers when gelation temperatures were **a)** 23 °C; **b)** 17 °C; **c)** -18 °C, *Images modified from* [29].

The structures created by phase-separation are well cross-linked and highly representative of ECM architecture. However, the application of this technique is limited to gelable polymers and the entire process can take weeks to complete [29].

1.3.7 Concerns with current fabrication methods

The existing methods covered above each suffer from one or more issues that prohibit them from being the ideal mechanism for generating aECM structures (see Table 1-1).

aECM Method	Drawbacks
Electrospinning	Restricted to polymers, requires careful control over solution viscosity
Laser spinning	Fibers too short, fibers not cross-linked
Self-assembly	Very complex, long processing times, post-processing required to cross-link fibers,
Phase-separation	Very long processing times, restricted to polymers, temperature and polymer concentration sensitive

Table 1-1 Existing nanofiber synthesis techniques for aECM fabrication and their drawbacks.

Clearly, value exists for a single-step technique that can quickly synthesize nanofibers from inexpensive materials, without the use of polymers, while simulating the highly cross-linked 3D architecture of ECM tissues and simultaneously displaying biocompatibility, and biodegradability.

1.4 Talking to cells: Nanoscale cues

As alluded to earlier, cells are widely affected by the micro and nanostructure of the materials they grow on, for example in their ability to adhere to surfaces [31], adsorb protein [32], or in their orientation [33]. Control over these abilities can result in a profound variety of outcomes, from inducing apoptosis (cell death), to better interaction with living tissue such as increased integration and reduced scar formation.

Structures that are constrained in the nanoscale in two of their three dimensions are considered to be one dimensional (1D). The morphologies of 1D nanostructures include rods, tips, belts, tubes, wires and fibers (please see Figure 1-11). Generally speaking, nanorods, nanotips, nanobelts, and nanotubes are constrained in length whereas nanowires and nanofibers have no such restriction. Despite such conventions, many structures inhabit regions across or between these morphological boundaries.

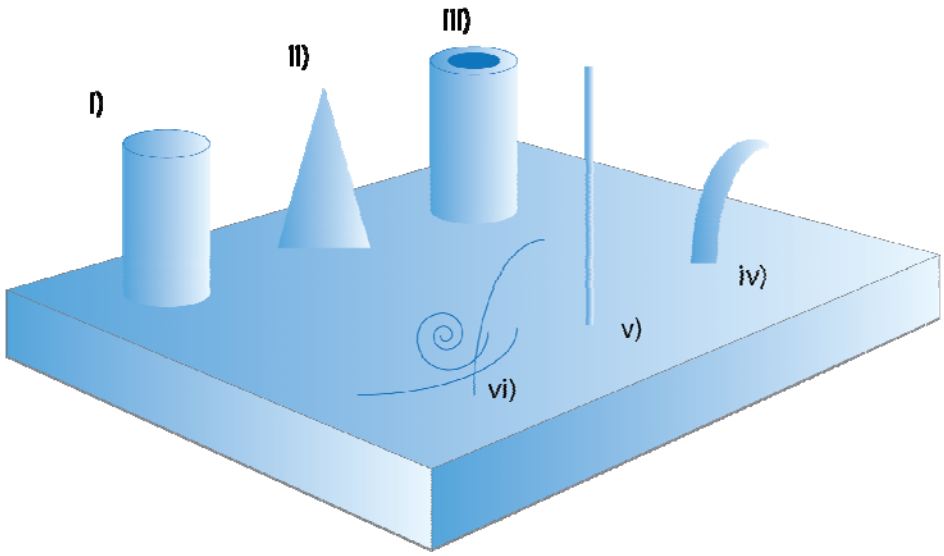

Figure 1-11 Morphologies of 1D nanostructures: **i)** nanorod; **ii)** nanotip; **iii)** nanotube; **iv)** nanobelt; **v)** nanowire; **vi)** nanofibers.

The work of Jiyeon Lee et al. has demonstrated that rod type structures on a variety of material surfaces reduce cell adhesion [31,34,35]. The increased hydrophobicity of material surfaces with tip type structures has also been shown [4,36]. Belt type structures have been synthesized from various materials and then functionalized with silver nanoparticles for use in antibacterial applications [37,38]; however, in these cases the active factor appears to be the material (silver is a well-known antiseptic and disinfectant) rather than the nanostructure itself.

The most popular methods for the nanostructuring of surfaces are techniques such as sol-gel, hydrothermal, solvothermal, galvanic displacement, and electrodeposition. These so-called

wet techniques have a number of drawbacks such as extended processing times, the use of hazardous organic solutions, which beyond being environmentally dangerous, may also result in chemically contaminated final products. Some dry-deposition systems have also been employed by researchers in their nanostructuring efforts; these are usually limited to radio frequency plasma assisted magnetrons, pulsed laser deposition and chemical vapor deposition (CVD). Such techniques must operate under vacuum conditions or in some cases require the use of catalysts, both of which can cause added complications in production scale up.

The definitive goal in nanofabrication is the ability to influence growth, geometry and size of nanostructures. To achieve this level of control, an understanding of a nanostructure's formation mechanism is required. A single technique that can generate the aforementioned types of nanostructures without the use of surfactants, catalysts, or pressure chambers exists today and it can produce these structures on inexpensive glass substrates.

1.5 Research Objectives

The morphological subsets of nanofibers and nanotips will be the focus of this thesis. Both of these nanostructures have previously been synthesized on various types of glass (nanofibers in particular on several different materials) by the Laser Micro Nano Manufacturing Lab at Ryerson University [39,40]. However, the composition and formation mechanism of the nanotips is unclear and the application potential of each nanostructure unexplored.

The thrust of this research work is to create two types of nanostructured surfaces from inexpensive, off-the-shelf, microscope slide glass via ultrafast laser ablation. Nanofibrous substrates that more closely resemble ECM tissues will be synthesized for testing as cell growth scaffolds. Congruently, nanotip substrates shall be synthesized as possible contra-cell surfaces.

2. Laser material interactions

2.1 Laser ablation

Laser ablation is the removal of material from a target object by incident laser light. The characteristics of this ablation are dependent on the wavelength, λ, of the laser light, the type of target material, and the intensity, I, of the laser beam.

2.1.1 Wavelength

The 'color' of a laser is defined by the wavelength of the output photons. Lasers span a wide gamut of wavelengths from the ultraviolet (200 – 370 nm), the visible (400 – 694 nm), to the infrared (700 – 1500 nm). However, the wavelength of light also determines the energy, E, of that light via the well-known energy relation,

$$E = \frac{hc}{\lambda} \tag{2-1}$$

where h is Planck's constant (6.626×10^{-34} J·s), and c is the speed of light in a vacuum (2.998×10^{8} m·s^{-1}) easily illustrates that as wavelength increases the energy of a photon decreases.

2.1.2 Absorption

Different target materials will have different absorption coefficients, α, that determine the amount of light absorbed by it. The inverse of the absorption coefficient, α^{-1}, will determine how far into a material particular wavelengths of light can penetrate. For example, materials that have low α will appear transparent. The relation is given as [41],

$$\alpha = \frac{4\pi k}{\lambda} \tag{2-2}$$

where k is the extinction coefficient of a material ($k > 0$ light is absorbed, $k = 0$ light travels losslessly forever). Thus choosing a wavelength that has a minimum absorption depth will allow for more efficient ablation.

2.1.3 Intensity

The intensity of a laser pulse can be calculated from the well-known equation,

$$I = \frac{4P}{f \tau_p d_0^2 \pi} \tag{2-3}$$

where P is the laser power, τ_p is the duration of the laser pulse (sometimes called pulsewidth), f is the number of such pulses per second (also called pulse frequency), and d_0 is the laser spot diameter.

The removal occurs when enough heat is absorbed by the target that material begins to melt or vaporize.

Just as the size of a shovel's blade will determine the smallest dimensions of a hole that can be dug, the wavelength of laser light will play a large part in determining the resolution of machined features. For a circular beam the smallest laser spot diameter, d_{min} is [41],

$$d_{min} = \frac{4l\lambda}{\pi D} \tag{2-4}$$

where l is the focal length of the lens, and D is the diameter of the beam incident on the focusing lens. Thus, the smaller the wavelength the smaller the spot size will be. Furthermore for beams with Gaussian profiles the diameter, d, will vary along the distance, z (also the direction of laser propagation), according to [41],

$$d(z) = d_{\min}\left(1+\left(\frac{\lambda z}{\pi\left(\frac{d_{\min}}{2}\right)^2}\right)^2\right)^{1/2} \quad (2\text{-}5)$$

When τ_p is measured in femtoseconds a laser can be classified as 'ultrafast', pulses of such duration are shorter than the time taken by a material to transfer energy from its electrons to its lattice and conduct heat [42]. Any energy in a single pulse that is not used in the ablation of material will dissipate out of the target zone. Maintaining the residual energy at ablation levels and thus enhancing the efficiency of ablation can be achieved by increasing the rate of pulses striking the surface. This accumulation of energy effect has allowed researchers to ablate poor thermal conductivity materials at pulse energies lower than the ablation threshold by simply using high pulse frequencies [43].

Through interactions with the surrounding environment and subsequent laser pulses the removed material can manifest as nanostructures. Before describing the formation mechanisms of these nanostructures, an understanding of the interactions between the laser and the target material is required.

2.2 Ultrafast laser ablation of glass

Ultrafast ablation of transparent dielectric materials (such as glass) occurs due to a nonlinear absorption process known as optical breakdown. Here, laser pulse energy is transferred to the free electrons of the target which then impact with and ionize the bound electrons of the target. As more bound electrons ionize more free electrons are generated and more electron impactions occur. This positive feedback process is sometimes referred to as avalanche ionization (see Figure 2-1a), and eventually, a critically dense plasma of free electrons is created.

The target material begins to breakdown when the electron plasma transfers its energy (in a matter of picoseconds) to the target lattice [44].

In cases where the laser intensity is high enough, multiple photons can be simultaneously absorbed by a bound electron and converted into a free electron. This multiphoton absorption process (see Figure 2-1b) can then seed enough free electrons for avalanche ionization to occur or, if threshold intensity is reached, can create critically dense electron plasmas to cause lattice breakdown. Due to the simultaneous occurrences of both processes it is difficult to untangle their individual contributions to the ablation process [42,44].

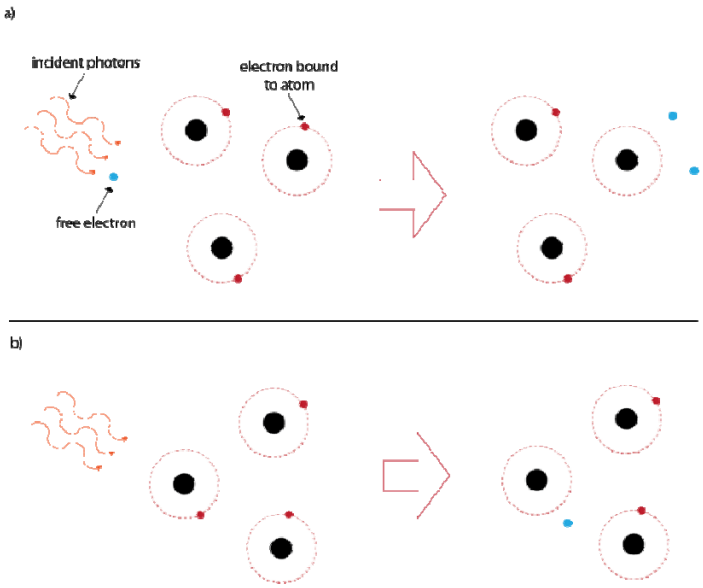

Figure 2-1 Nonlinear ionization processes in femtosecond laser ablation include **a)** avalanche ionization; and **b)** multiphoton absorption.

Multiple laser pulses create an accumulation of energy within the material lattice and eventually the binding energy of electrons and atoms are surpassed and they leave the surface of the target in an expanding plume. The broken atomic bonds loosen the lattice and as further energy is absorbed material phase changes are instigated. Vaporization, melting, and exfoliation of the target material will all occur, each contributing to the generation of micro and nanostructures [45-47].

2.2.1 Vaporization and the ablation plume

When the laser energy absorbed by the target material exceeds the binding energy of the lattice vaporization of the material surface may occur. Much research has been focused on characterizing and understanding the dynamics of the vapor formed plasma generated by laser ablation. Of particular interest to researchers is the interaction of the vaporized species ejected from the target (laser ablation plume) with the background (ambient) gas. The motivating force is the importance of the plume-gas interaction in the formation and growth of nanoparticles.

By using an intensified charge coupled device (ICCD) to capture high speed images (resolution of 1 ns), Harilal et al. showed that the expansion behavior of the ablation plume from a single laser pulse is dependent on ambient gas pressures [48]. At low pressures ($\leq 10^{-2}$ Torr) plasma expands freely (see Figure 2-2a), above 0.1 Torr the plasma and gas begin to mutually penetrate and this may split and sharpen the plume (see Figure 2-2b), finally at pressures beyond 10 Torr the plume flattens and the interpenetration zone contracts (see Figure 2-2c).

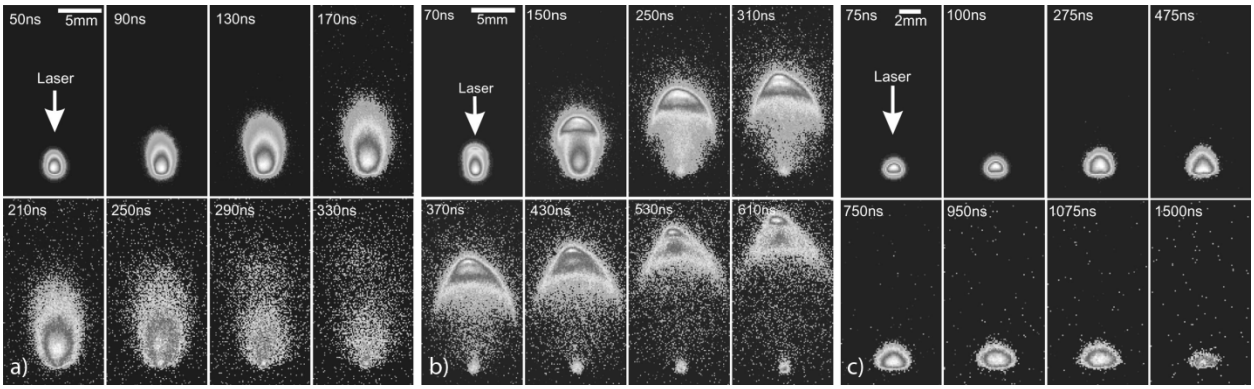

Figure 2-2 Plume expansion behavior with ambient gas pressure at **a)** 1 x 10^{-2} Torr; **b)** 0.15 Torr; and **c)** 100 Torr, *Images modified from* [48].

The ICCD imagery also reveals the timescale behavior of the plume. In the early stages (< 40 ns) the plume is practically linear regardless of background pressure. At the middle stages (< 500 ns) and at moderate pressures the plume expansion can be modeled as a spherical

shockwave. At the end stages (> 500 ns) the plume interacts heavily with the background gas, slowing considerably and may be approximated by a drag model.

Interestingly, other researchers have attempted to show that the expanding plume removes ambient gas and the two locate exclusively (i.e. they do not mix) [49]. Testing at two wavelengths (1064 and 355 nm) Sasaki et al. concluded that, after ablating a target with a single pulse, mixing did not occur. The researchers further postulated that according to these results the chemical interactions between plume and gas can only occur at the interface between plume and ambient gas. However, by measuring the density distribution of the reaction product it was shown that while ablation at 1064 nm was consistent with the expectation, ablation at 355 nm was not.

As the expanding plasma front cools in its interaction with the ambient gas, vapor species begin to collide and condensation occurs. The newly formed particles continue to interact with and aggregate into larger nanoscale structures [45].

2.2.2 Melting

The laser energy left over after vaporization occurs will result in material heating and the creation of a melt layer. At this point several processes can occur that result in spherical particle formation.

Rapid cooling and heating due to the laser pulses can create finger-like projections of molten material (typically tens of nanometers in diameter) [46]. Eventually molten material will separate from the substrate surface and form small particles. These particles are said to be formed due to hydrodynamic sputtering and well below micrometer-sized.

The vapor plume described in the previous subsection can also result in a secondary mechanism for particle formation. As the high temperature and pressure plume expands it may

push melted material outward from the center of the irradiated area forming a raised rim. This back-coil pressure can cause microspherical particles to be ejected and is typically evidenced by the formation of a crater after the melted surface cools [46,47].

In cases where the surface region overheats past the point of thermodynamic stability the molten layer rapidly switches into a combination of vapor and liquid droplets [31]. This process is referred to as explosive boiling and typically thought to be the result of bubbles formed by the density fluctuations of the superheating molten layer. Explosive boiling is considered to be the primary mechanism in ultrafast laser ablation and the size of the ejected particles are thought to be limited only by the thickness of the molten layer of target material [46].

2.2.3 Exfoliation

Thermal expansion and stress of a target material by the incident laser beam can result in the fracturing of the solid and result in another form of material removal [46]. The fracture-induced generation of particles is called exfoliation and especially significant in refractory, brittle materials. Such particles are usually quite large and irregularly shaped, often cleaving along a material's crystallographic planes. Spallation may occur when the same laser induced stresses acting on metastable fluids results in cavitation and fragmentation leading to the ejection of large spheres many microns in size.

2.3 Summary

The process of laser ablation involves very complex physics that has yet to be completely understood. The characteristics of the laser, (such as wavelength, intensity and, beam size), the nature of the target material (absorption coefficient) and ambient conditions (gas pressure) can affect the quality and quantity of ablation. In the ensuing removal of material, several particle

generation mechanisms occur during the vaporization, melting, and exfoliation of the target material. This results in the formation of nano to micro scaled features and structures.

3. Experimental procedures

3.1 Experimental setup

The experimental setup, as illustrated in Figure 3-1, consists of a 1030 nm wavelength direct-diode pumped Yb-doped fiber-amplified ultrafast laser source, a beam delivery system, a computer controlled galvoscanner and a 3-axis micrometer-resolution translation stage. The laser is capable of delivering pulses with a 200 fs duration, pulse frequencies in the range of 200 kHz to 26 MHz, all at a maximum average power of 15 W. The time spent delivering laser pulses to a single point on a sample (dwell time) is controlled via an acousto-optical modulator. Experiments were performed at pulse frequencies of 8.4, 12, and 25 MHz and dwell times of 2, 5, and 10 ms. The galvoscanner enabled the samples to be irradiated with a predetermined laser scan pattern, in this case, an array of points with a center-to-center distance of 50 or 100 μm. The beam is measured to be 8 mm in diameter as it enters the lens of the galvoscanner. Given an effective focal length of 63.5 mm for this lens, the spot size of the beam at the sample is calculated from Equation 2-4 to be 10.38 μm. All samples were processed under ambient conditions. Some experiments (see section 4.2 and 4.3) were performed with nitrogen gas flowing at a rate of 10 SCFH directly over the ablation site perpendicularly to the propagating direction of the laser beam. Additionally, for a small subset of experiments (see section 4.3) a second direction of gas flow was tested, 45° to the propagating direction of the incident laser beam.

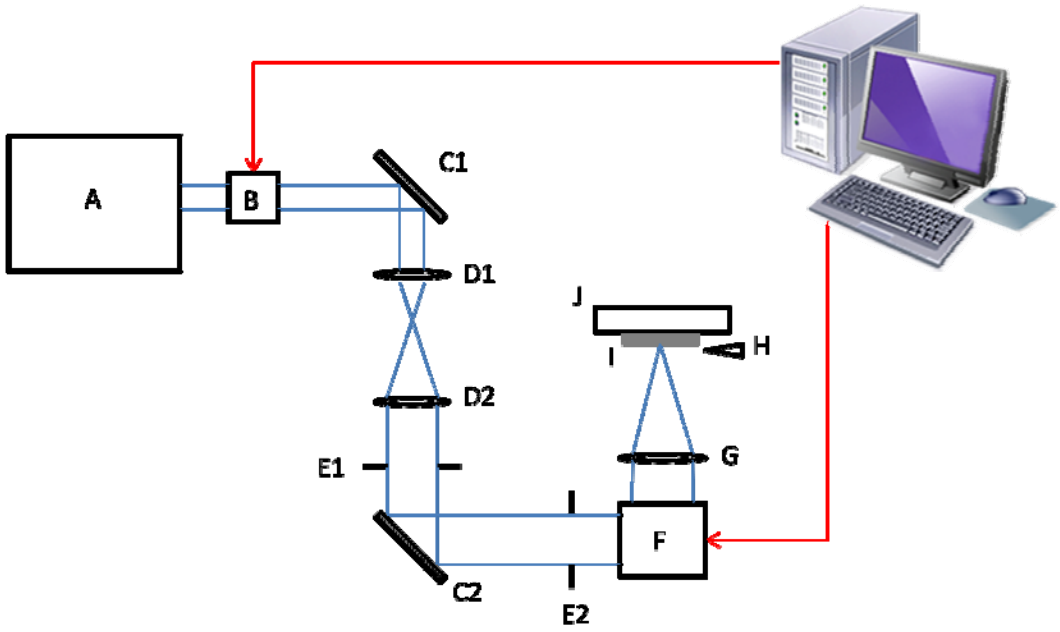

Figure 3-1 Schematic diagram of experimental setup. **A**, ultrafast laser source; **B**, acousto-optic modulator; **C1** and **C2**, mirrors; **D1** and **D2**, beam expander; **E1** and **E2**, diaphragms; **F**, galvoscanner; **G**, telecentric lens; **H**, nitrogen nozzle; **I**, sample; and **J**, 3-axis stage.

3.2 Ablated sample preparation and characterization

Glass samples were cut from standard 75 x 25 mm Corning soda-lime glass microscope slides (72% SiO_2, 15% Na_2O, 5% CaO, 4% MgO, 2% Al_2O_3, 1% K_2O, 1% all other constituents). After laser processing, samples undergoing material characterization were sputter coated with gold and then examined under a scanning electron microscope (SEM). Several samples were sputtered prior to laser processing to determine the effect, if any, of a gold thin film on nanostructure formation. For higher resolution observation, copper substrate grids were dragged across the surface of ablated samples to collect the nanostructures and subsequently observed with a transmission electron microscope (TEM). For chemical characterization of the nanostructures, energy dispersive X-ray (EDX) analysis was employed.

3.3 Cell culture and characterization

All procedures involving live cell handling were performed in a Level 2 Biosafety certified laboratory. Six passages of NIH 3T3 mouse embryonic fibroblast-type cells were grown in tissue culture flasks (BD Falcon, Massachusetts, USA) with a cell media solution of Dulbecco's Modified Eagle's Medium with 10% fetal bovine serum (FBS) and 1% streptomycin-penicillin antibiotic and incubated at 37 °C in a 5% CO_2 atmosphere. Cells between the third and sixth passage were used for seeding after growing to at least 70% confluence.

Ablated glass samples and unprocessed control samples were first sterilized under ultraviolet (UV) light for 15 minutes before being seeded at a density of 1 x 10^5 cells·mL^{-1}. The seeded samples were then incubated for varying periods of 12 hrs, 1 day, or 1 week. After incubation the cells were fixed to the substrates with a 2.5% concentration of glutaraldehyde diluted in Sorensen's Phosphate Buffer. The specimens were then dehydrated in increasing concentrations (75%, 90%, and 100%) of ethyl alcohol before transferring to a critical point dryer. The now preserved samples were then sputter coated with gold and examined using SEM and EDX techniques.

4. Nanostructure formation

4.1 Introduction

The exploration of laser parameter influence upon nanofiber formation on various substrates and the mechanisms of their formation has already been extensively studied by the Laser Micro Nano Manufacturing Lab at Ryerson University [39,50]. However, much remains to be understood about the growth and composition of laser synthesized nanotip structures on glass. Therefore, emphasis was placed on gleaning insight into tip rather than fiber formation.

4.2 Nanotips

Ultrafast laser ablation of soda-lime glass substrates was used to synthesize nanotips that grew in flower-like arrangements. The relationship between laser parameters and nanotip morphology was explored. The composition of these nanotips was also investigated. In concert with the morphological and compositional findings, a new formation mechanism was proposed.

4.2.1 Morphology of nanotips

All nanotips were randomly oriented and displayed a characteristic tapered morphology, broad at the base with a distribution of widths from 100 nm to 2 μm and narrowing to a head as small as 20 nm over a length of 1 μm to 10 μm. At a pulse frequency of 8.4 MHz, increasing the dwell time resulted in a greater number of thinner, but not longer, needle-like tips (see Figure 4-1). The base width of tips at 2 ms and 5 ms dwell times were typically 1-2 μm with more tips per flower generated at 5 ms. When dwell time was increased to 10 ms base widths shrank to between 100-500 nm. Interspersed among and around the nanotips were nano and microscale spheres. In some cases, aggregated nanoparticles were also observed.

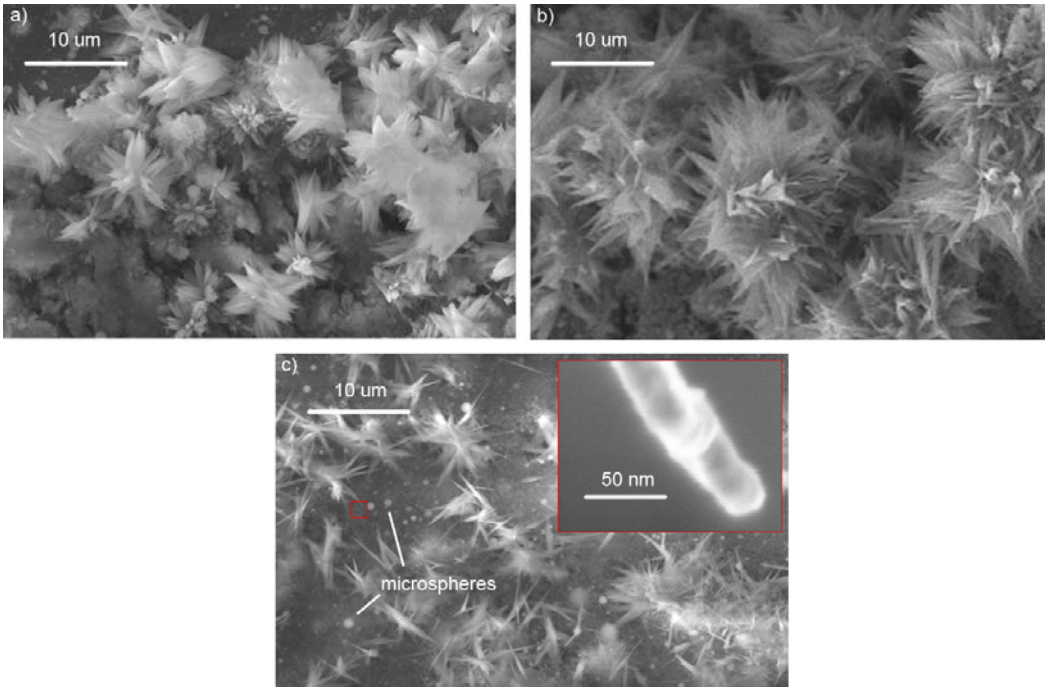

Figure 4-1 SEM micrographs of flower-like nanotips formed at a pulse frequency of 8.4 MHz and dwell times of: **a)** 2 ms; **b)** 5ms; **c)** 10 ms, inset shows high magnification image of a typical single 10 ms dwell time nanotip with a head width of 20 nm.

Also, at this pulse frequency nanotip flowers often formed in clusters of 50 μm or larger, however, dramatic differences in nanotip population density (nanotips per unit area) were seen, oftentimes within a single ablated region of a sample (see Figure 4-2).

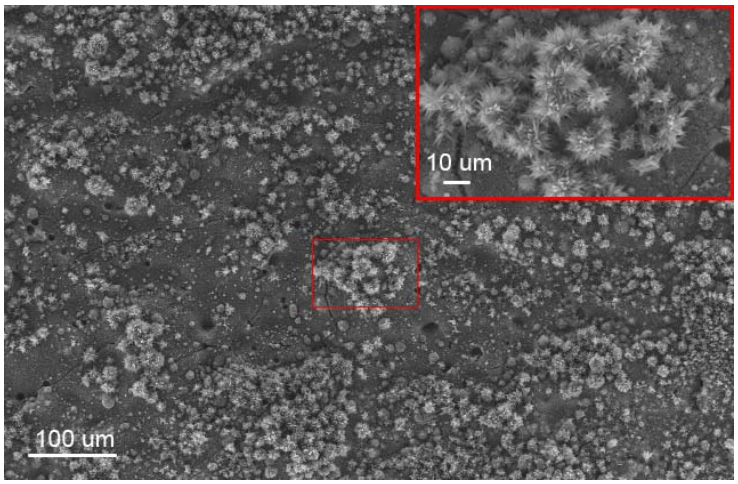

Figure 4-2 SEM micrograph of many clusters of flower-like nanotips, inset shows higher magnification of a typical cluster.

When the pulse frequency was increased to 12 MHz (see Figure 4-3) single nanotips were observed at 2 ms dwell time and at 5 ms dwell time the formation of flower-like nanotips was more prevalent along with microsphere formation and melt splatter. At 10 ms dwell time there was further evidence of microsphere formation and melt splatter alongside continued flower-like nanotip formation. However, at all dwell times, clusters of flower-like nanotips as observed at the lower laser pulse frequency were not present.

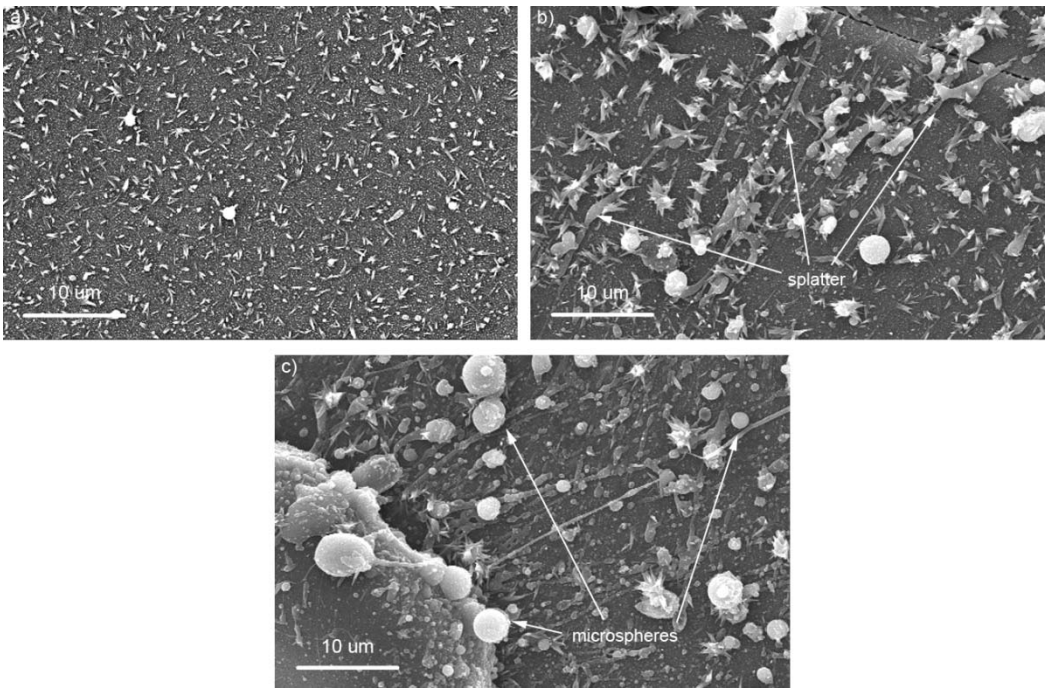

Figure 4-3 SEM micrographs of single nanotips formed at a pulse frequency of 12 MHz and a dwell time of **a)** 2 ms; and flower-like nanotips at dwell times of: **b)** 5 ms; and **c)** 10 ms.

At pulse frequencies of 25 MHz, nanotip formation was typically non-existent at 2 ms dwell time and sporadic at 5 and 10 ms (see Figure 4-4).

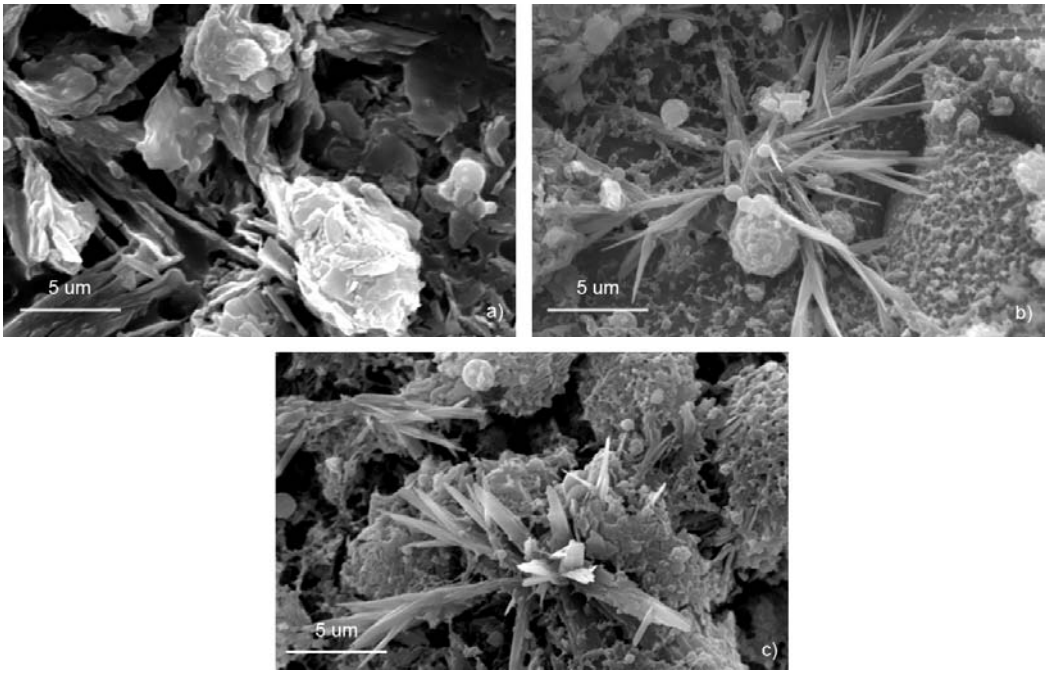

Figure 4-4 SEM micrographs of glass substrates after ablation at a pulse frequency of 25 MHz and dwell times of: **a)** 2 ms, showing no nanotip formation; **b)** 5 ms; and **c)** 10 ms showing rare occurrences of flower-like nanotips.

4.2.2 Composition of nanotips

Analysis of the flower-like nanotips revealed that the composition of the structures were different from that of the surrounding substrate. Presented in Figure 4-5 are EDX area scans of a cluster of flower-like nanotips (the region bounded in red on the SEM image and white on the EDX area scans) surrounded by aggregated nanoparticles (the area outside the boundary). This nanotip region shows high concentrations of oxygen and sodium and a clear absence of silicon.

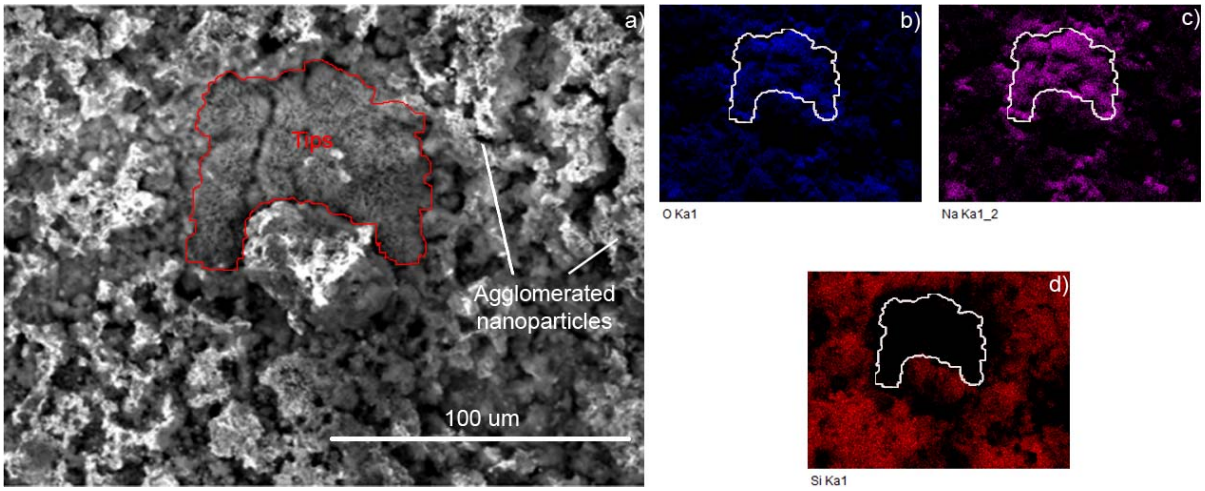

Figure 4-5 SEM micrographs of: **a)** cluster of flower-like nanotips and surrounding nanoparticle agglomerates with corresponding EDX area scans: showing high concentrations of **b)** oxygen; **c)** sodium; and an absence of **d)** silicon within the bounded nanotip region.

The destructive nature of mounting samples on the substrate grid for use on the TEM resulted in the collection of nanotip fragments. Inspection of individual fragments using line scan EDX revealed that they consisted primarily of oxygen and sodium. Sharp silicon (Si) peaks correspond to aggregates of Si nanoparticles (see Figure 4-6). The linescans were purposely drawn well beyond the boundaries of the nanotip so as to compare the element levels of the nanotip to that of the TEM grid. Since the levels of silicon are completely in the noise range except at the two indicated points of interest we can deduce that silicon is certainly not present throughout the tip.

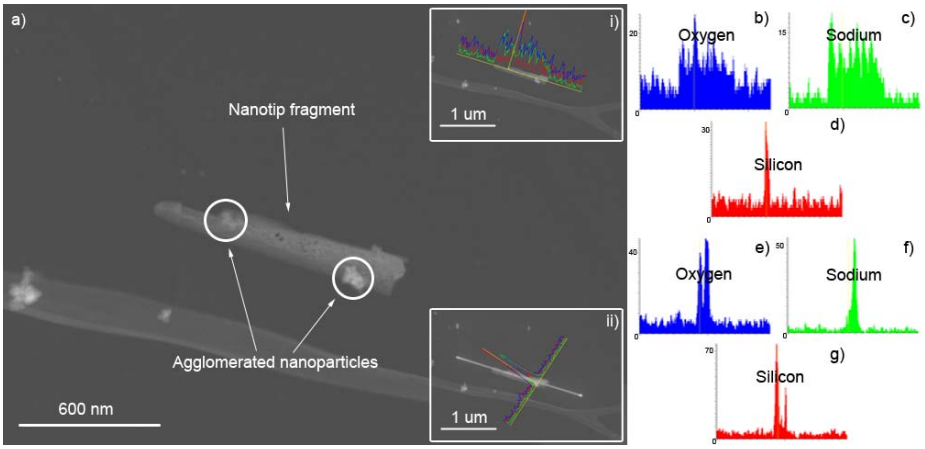

Figure 4-6 TEM micrographs of: **a)** collected nanotip fragment and linescan EDX along: **i)** length, which shows; **ii)** width of fragment. EDX results along the length and width show: **b)**, **e)** oxygen; **c)**, **f)** sodium throughout the fragment; **d)**, **g)** silicon only at the agglomerated particles.

Collected along with large amounts of nanotip fragments were microspheres. EDX area scans (see Figure 4-7) show that the spherical structures differed considerably in composition from their surrounding tips. The spherical particles were primarily constituted of silicon, calcium, aluminum and magnesium. This was starkly evident in an EDX area scan which showed a dearth of sodium and oxygen in the microsphere.

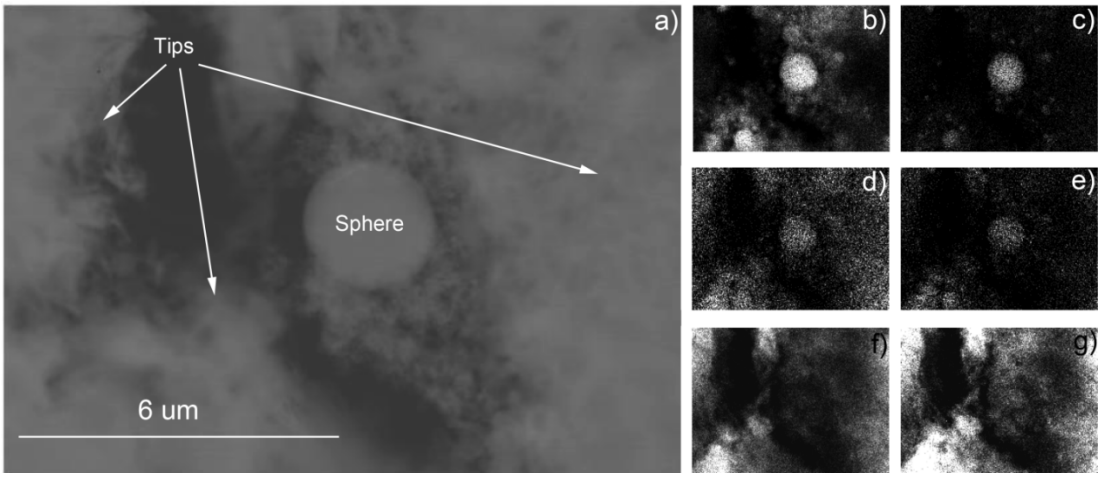

Figure 4-7 TEM micrograph of: **a)** nanotip fragments and microspheres with corresponding EDX area scans showing the composition of microspheres to be primarily: **b)** silicon; **c)** calcium; **d)** aluminum; and **e)** magnesium while nanotips are composed of: **f)** sodium; and **g)** oxygen.

4.2.3 Ionization of nitrogen

Given the values of the laser parameters used in this experiment the calculated intensity from Equation 2-3 for pulse frequencies of 8.4, 12, and 25 MHz are 1.1 x 10^{13}, 7.0 x 10^{12}, and 3.5 x 10^{12} W·cm^{-2} respectively. The first and second values are well within the threshold intensity for nitrogen ionization (~3.5x10^{12} W·cm^{-2}) [51]. However, the calculated intensity at a pulse frequency of 25 MHz is at the cusp of the ionization threshold. The values calculated here are for an ideal system and of course, further reductions in intensity should be expected from optical losses.

At 8.4 MHz the calculated laser intensity at the focus would ionize nitrogen at a rate of 10^{7} s^{-1} [51] but falls as a function of height above the focal plane due to the increased laser spot diameter. From Equation 2-5 it can be deduced that at a distance of 10 μm above the focal plane the beam intensity drops by ~10 % resulting in a tenfold decrease in the rate of nitrogen ionization. At a distance 130 μm above the sample surface the beam diameter expands to 20 μm and the beam intensity is too low to ionize nitrogen. As shall be explained in the next section, this layer of ionized nitrogen may play a critical role in the formation of nanotips.

4.2.4 Proposed formation mechanism

The presence of several types of structures (single/clustered nanotips, microspheres, and nanoscale aggregates) would appear to indicate multiple formation mechanisms at work. The Si formations on nanotip fragments observed under TEM are evidently the result of aggregating nanoparticles and are usually attributed to nucleation and condensation of vaporized material. In this process, beams of sufficiently high laser fluence heat the region of a target material and vaporize atoms and molecules creating a plasma. This plasma will expand as a plume due to continued heating by the laser. The vapor plume begins to cool as it propagates outward

interacting with the ambient environment and as a result, the vaporized atoms condense and particles begin to aerosolize (see Figure 4-8 ii). The particles may then continue to collide with each other forming larger nanoscale aggregates.

The micro-scale spherical particles generated in this study are indicative of formation from a liquid state. Furthermore, the compositional differences between the microspheres and the nanotips in our experimental results point to a phase separation taking place. It is highly likely then, that the molecules separate by density (see Table 4-1).

Molecule	**Density ($g \cdot cm^{-3}$)**	**Wt. %**
Na_2O	2.270	14
SiO_2	2.2 – 2.6	73
CaO	3.3	7
MgO	3.580	4
Al_2O_3	4.000	2

Table 4-1 Soda-lime glass composition by weight and corresponding molecular densities at 25 °C

Depending on their size (1-20 μm), these spherical particles can be attributed to spallation, backcoil pressure, and explosive boiling mechanisms. In the first scenario, after a melt layer is created (see Figure 4-8 iii), tensile stresses induced by the laser create defects (cavities) along the solid-melt interface, these defects combine causing the ejection of droplets. The plume of plasma described earlier is closely related to a second mechanism; since the plume expands radially in all directions the plume's downward expansion, or backcoil pressure, pushes liquid melt out from the irradiated spot. If the momentum of the melt is higher than the surface tension, droplets will be ejected around a formed rim as shown in Figure 4-8 vii. Finally, explosive boiling (sometimes termed phase explosion) occurs when the ablated material is heated past the point of

its thermodynamic stability; in this situation the superheated liquid will generate vapor bubbles that, after reaching a critical radius, eject both vapor and liquid droplets.

Sodium oxide is the least dense compound in soda-lime glass. Therefore, regardless of the melt ejection process we can expect sodium oxide to be at the melt surface (see Figure 4-8 iv). Furthermore, Na_2O is a polar molecule. The previously described layer of ionized nitrogen may cause an electrostatic effect that attracts the polar liquid phase Na_2O (see Figure 4-8 v). As this liquid is drawn out towards the nitrogen ions it cools and solidifies into nanotips. The drawing process is evidenced by the tapered structure of the nanotips (see Figure 4-8 vi). In this experiment the nitrogen gas was provided from one nozzle and in only one direction. As laser dwell time increases, the population of nitrogen ions would grow (see Figure 4-8 vii). This increase in ions would offer more sources of electrostatic attraction for the polar Na_2O. Thus, a greater number of tips would be drawn from a droplet of the same volume; the formed cluster would have a higher density of tips but they would be thinner in width. However, this increased ion density does not affect the length of the nanotips (see Figure 4-8 viii).

The formation of nanotips into clusters larger than the beam diameter (see Figure 4-8) suggests that the ionization of nitrogen has an expanded area of effect; which can be accounted for by the constant flow of nitrogen disturbing the population of ions and moving them away from the ablation zone. The fewer observed flower-like nanotips at 12 MHz pulse frequency is congruent with a lower quantity of ionized nitrogen due to the lower laser pulse intensity. The observed scarcity of nanotips at a 25 MHz pulse frequency can be explained by little to no nitrogen ionizing due to the laser pulse intensity dropping below the ionization threshold of nitrogen.

We have previously shown [52] that without nitrogen flow, similar ablation conditions will not result in nanotip but rather nanofiber formation. Given that the threshold intensity for ionization of air is lower than that of nitrogen [51,53], this may seem surprising. However, the high pressure plume formed during vaporization creates a shockwave that pushes the ambient gas away from the site. Thus, the ablation zone would be devoid of ionized air. The introduction of nitrogen flow during the ablation process forces a mixing of nitrogen gas into the plume. The nitrogen flow also results in rapid cooling, which would aid in halting the vaporization process and initiating melt ejection processes.

Although silicon dioxide (SiO_2) is similar in density to Na_2O, the SiO_2 molecules are non-polar and therefore unaffected by the electrostatic effect, hence the lack of silicon in the nanotip structure. However, this explanation would not hold true for highly ionic calcium oxide molecules (CaO). The higher density of CaO must impede its ability to be drawn into nanotip structures. Melt that has not solidified into nanotips is likely low in Na_2O; a delayed melt expulsion process (such as backcoil pressure or explosive boiling) would then explain the formation of spherical particles rich in SiO_2 and higher density molecules (see Figure 4-8 ix). The crater and rim structures are typically evidence of both explosive boiling and backcoil pressure events with microspheres and nanotip clusters around the rim (see Figure 4-8 x).

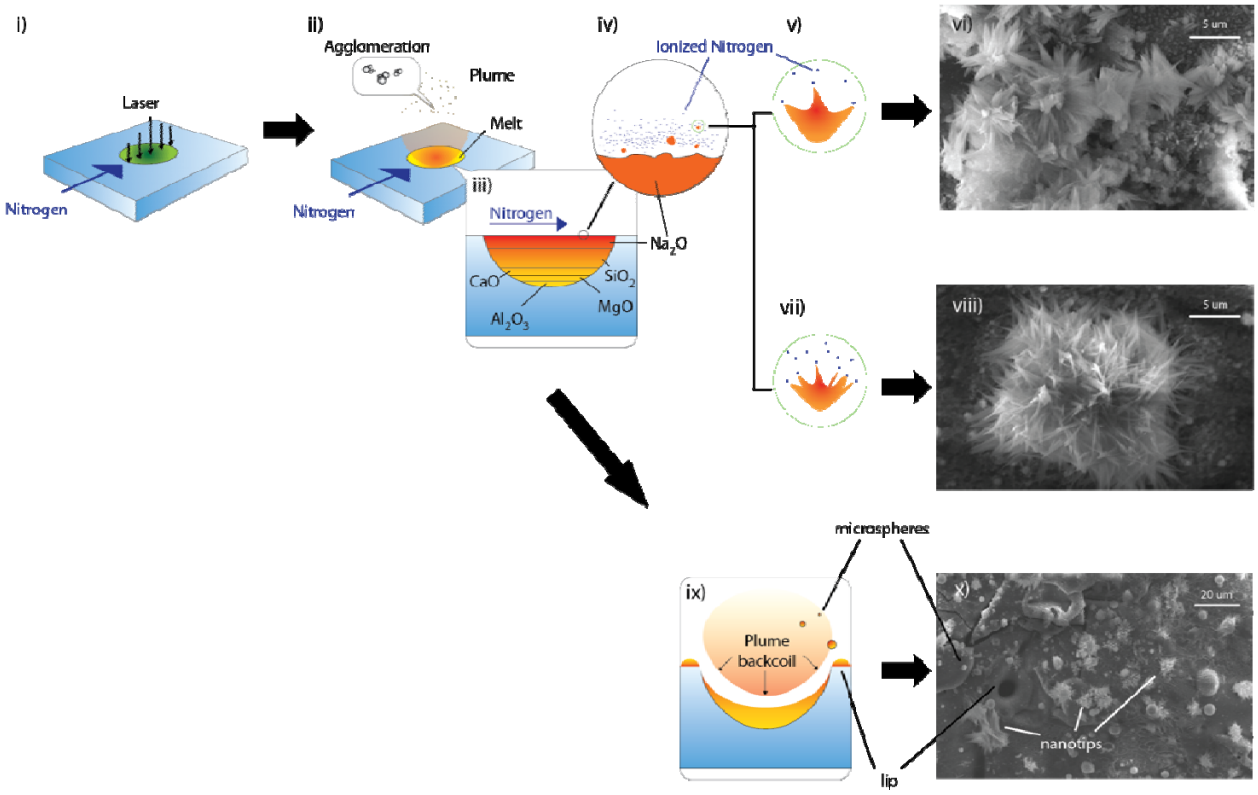

Figure 4-8 The proposed formation mechanisms: **i)** laser pulses induce optical breakdown; **ii)** agglomeration of Si nanoparticles occurs in the plume and a melt layer forms; **iii)** melt layer separates soda-lime glass molecules by density; **iv)** spallation creates microscale Na_2O melt spheres; **v)** polar Na_2O molecules are electrostatically drawn out towards the laser-ionized nitrogen; **vi)** the drawn Na_2O cools into flower-like nanotip arrangements (dwell time = 2 ms); **vii)** at longer dwell times more nitrogen is ionized; viii) resulting in thinner nanotips (dwell time = 10 ms); **ix)** melt that is now low in Na_2O is expelled via plume backcoil pressure to form melt spheres composed of the higher density molecules; **x)** typical crater and characteristic lip indicative of a backcoil pressure event (dwell time = 2 ms).

4.3 The effect of gold on nanotip synthesis

A brief set of ablation experiments were also conducted on gold sputter coated glass samples at a pulse frequency of 8 MHz, dwell times of 2 and 10 ms, center-to-center laser spot spacings of 50 and 100 µm, and nitrogen nozzle angles of 90° and 45° (measured from the incident laser beam). The generated structures appeared to be curved and belt-like rather than the previously observed nanotips.

4.3.1 Morphology of curved nanotips

At a nozzle angle of 90°, decreasing the laser spot spacing and increasing the laser dwell times resulted in higher densities of curved nanotip formation (see Figure 4-9). Furthermore, ablation at the closer spot spacing appeared to provide thinner nanotips on average with tip widths decreasing from about 400 to 200 nm.

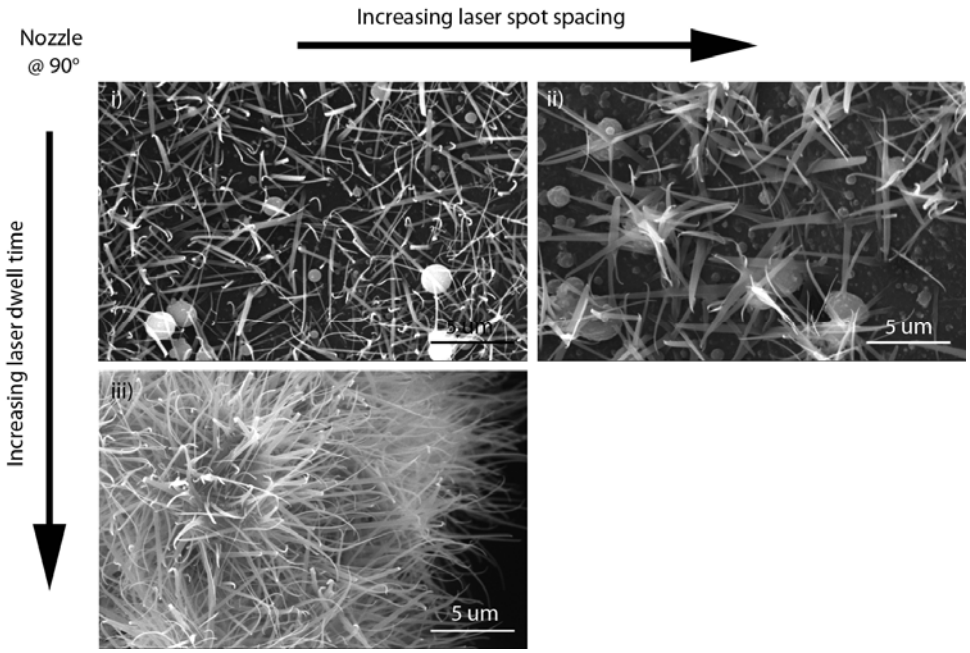

Figure 4-9 SEM micrographs of nanobelts formed with nitrogen introduced to ablation zone at 90° and at dwell times and spot spacings of: **i)** 2 ms & 50 μm; **ii)** 2 ms & 100 μm; **iii)** 10 ms & 50 μm.

When the nozzle angle was changed to 45° (see Figure 4-10), decreasing the laser spot spacing at 2 ms dwell time appeared to result in very wide tips (about 600 nm on average) but also the generation of visible amounts of agglomerated nanoparticles. Increasing the dwell time to 10 ms resulted in thinner tips of approximately 400 nm and much melted debris.

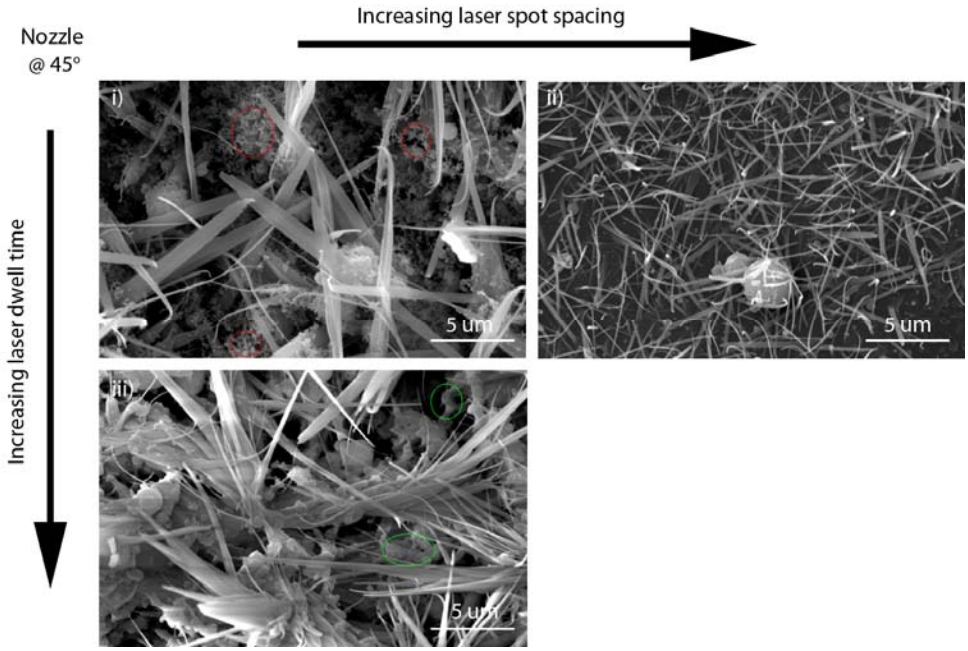

Figure 4-10 SEM micrographs of nanobelts formed with nitrogen introduced to ablation zone at 45° and at dwell times and spot spacings of: **i)** 2 ms & 50 μm, red ovals indicate some areas of nanoparticle agglomeration; **ii)** 2 ms & 100 μm; **iii)** 10 ms & 50 μm, green ovals indicate some areas of melted debris.

EDX measurements taken over the nanotip growth region show increased levels of sodium compared to unablated regions (see Figure 4-11). This suggests that the composition of the curved nanotips is similar to that of regular nanotips.

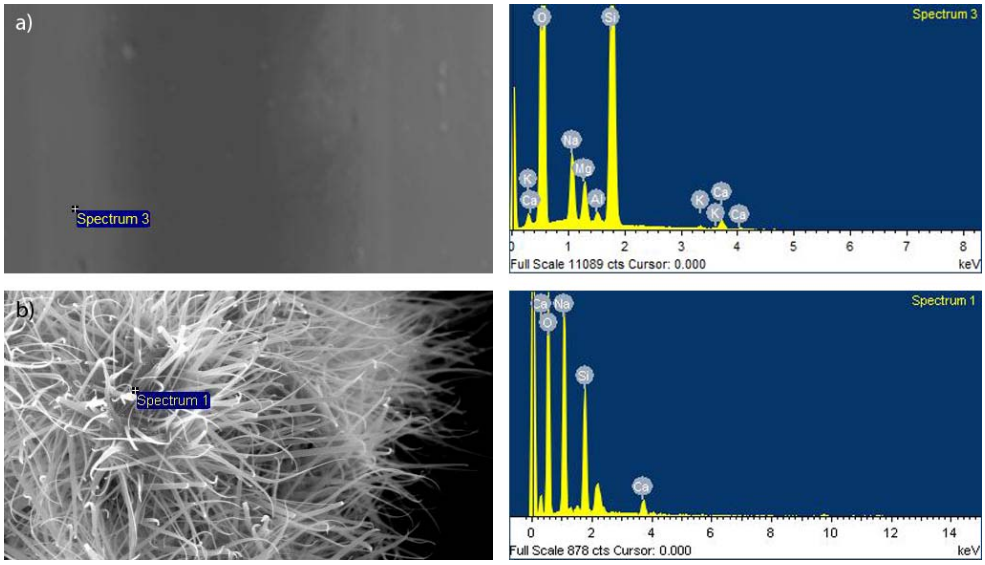

Figure 4-11 SEM micrographs along with their EDX spectra of **a)** unablated glass; **b)** curved nanotips showing an increase in sodium content.

4.3.2 Potential formation mechanism

The sputtered gold layer may result in two phenomena. Firstly, when compared to bare glass, the metal atoms must provide more free electrons for the nonlinear ionization processes that instigate femtosecond ablation. Secondly, the gold atoms may act as catalyst sites for nanobelt growth. Confirmation of a catalytic mechanism would require the detection of a gold particle on the belt structure.

The nanoparticle agglomeration that occurs at the 45° nozzle angle may indicate that more vaporization and less melt expulsion took place during ablation. This could imply that at this angle the nitrogen flow interacts heavily with the plasma front but not the ablation surface. This would result in a lower rapid cooling effect of the surface, reducing melt expulsion processes but allowing for more condensation of nanospecies within the plume. The melted debris seen at the longer dwell time could be the remnants of re-melting nanoparticle agglomerates.

4.4 Nanofibers

When ablation experiments were performed using the same laser parameters that generated nanotips, but without the presence of nitrogen gas flow, the resulting nanostructures were fibrous formations. All fibers for this study were created at a pulse frequency of 8 MHz, 10 ms dwell time, and spot spacing of 0.05 μm.

4.4.1 Morphology of nanofibers

The SEM micrographs of the ablated surfaces (please see Figure 4-12) show lightly packed, highly interconnected nanofibrous strands. The porous appearance of the laser treated surface is a result of the loose organization of the nanofibrous strands into loop-like substructures of diameters varying from hundreds of nanometers to several microns. At higher magnification individual spherical nanoparticles can be distinguished that clearly aggregate into cross-linked nanofibrous strands. The nanoparticles range in diameter but are typically smaller than 100 nm.

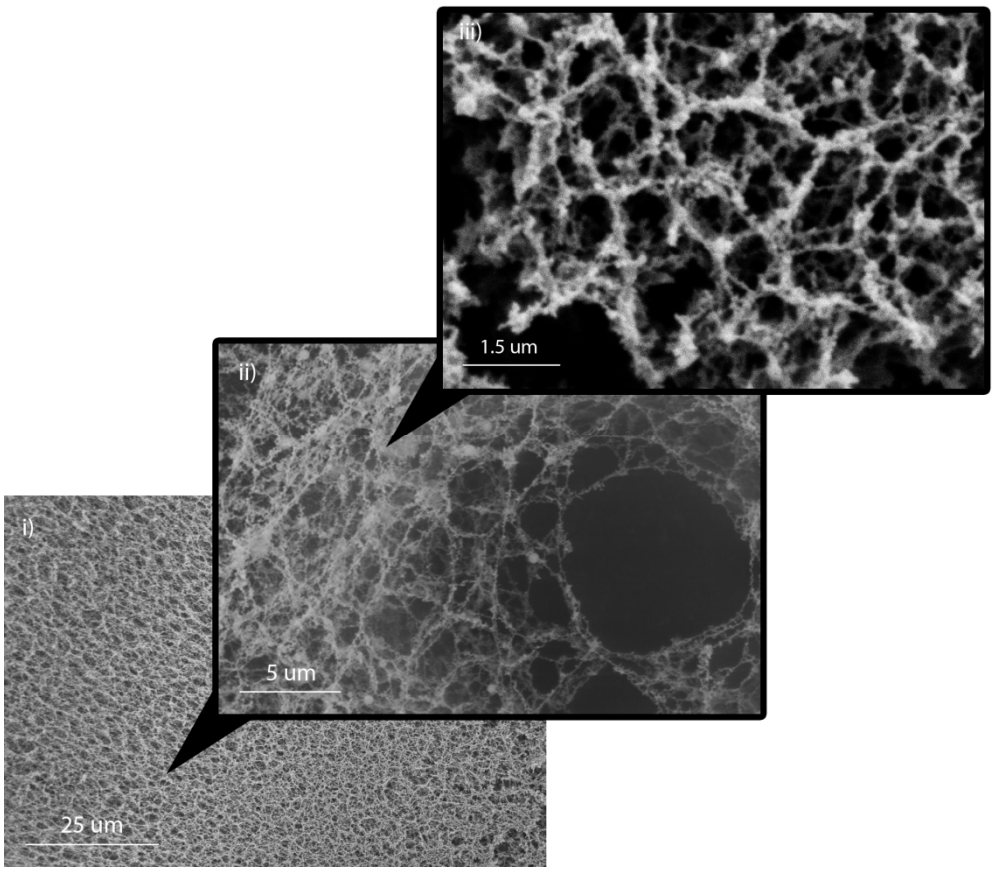

Figure 4-12 Representative SEM micrographs of increasing magnification showing the **i)** porous appearance of ablated surface; **ii)** organization of highly interconnected nanofibrous strands into loop-like structures; **iii)** strands consisting of individual nanoparticles.

4.4.2 Composition of nanofibers

Synthesized nanofibrous regions were isolated on TEM grids, and their constituent nanoparticles observed under SEM and then examined using EDX (see Figure 4-13). As area scans show, the nanofibers are composed primarily of silicon oxide nanoparticles. The gold readings are from the sputter coating given to the sample prior to imaging, and the copper signal represents the TEM substrate that the nanoparticles were collected on.

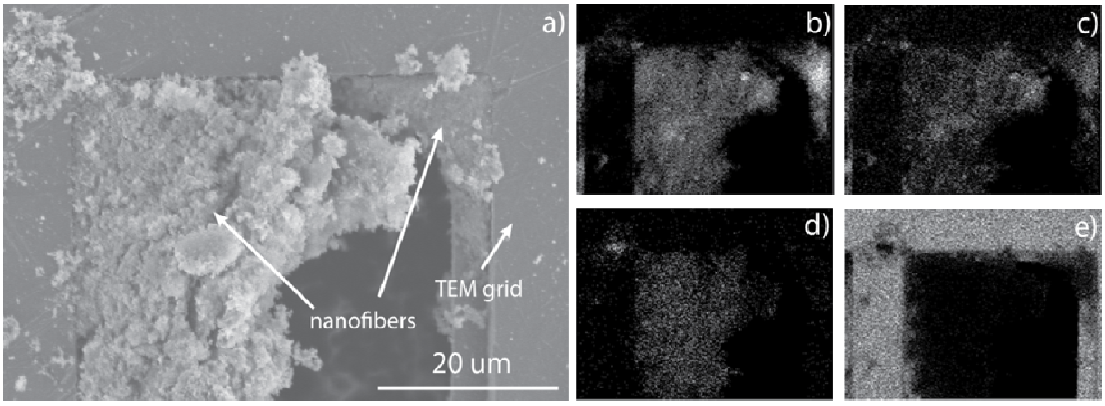

Figure 4-13 SEM micrograph of: **a)** nanoparticle constituents of nanofibers with corresponding EDX area scans showing the composition of nanoparticles to be primarily: **b)** silicon; and **c)** oxygen with a **d)** gold sputter coating; and the TEM grid represented by **e)** copper.

4.4.3 Formation mechanism

As discussed earlier in section 4.2.4, given the composition and morphology of the observed nanoparticles, the vapor condensation of laser-induced plume particulates and subsequent agglomeration via collisions is the likeliest process by which the 3D networked nanofibers are synthesized. Without the presence of nitrogen the rapid cooling and melt expulsion processes of laser ablation are probably minimized further encouraging material vaporization [40].

4.5 Summary

Two distinct nanoscale structures can be generated via laser ablation of soda-lime slide glass. In the presence of a nitrogen flow over the ablation area, nanotips can be synthesized and their widths controlled via the laser dwell time parameter. When nitrogen is not used nanofibrous structures can be synthesized out of agglomerating spherical nanoparticles.

The composition of nanotips is different from that of nanofibers. Nanotips are Na_2O structures whilst the nanoparticles that combine to form the nanofibers are SiO_2. Based on this evidence and the observation and compositional analysis of other microstructures present after

the ablative process, a novel formation mechanism for nanotips has been proposed. This mechanism involves the laser ionization of nitrogen gas that electrostatically attracts polar Na_2O molecules that have been liberated from the substrate in what is likely a melt expulsion process.

When a thin layer of gold was deposited on the glass substrate prior to ablation curved nanotips were synthesized. The formation mechanism of this nanostructure is not well understood. However, as their composition is similar to ordinary nanotips the process behind curved nanotip synthesis may likewise be comparable.

The mechanism behind nanofiber formation is the well-known vapor condensation process where a plasma of vaporized molecules and atoms aerosolize in the violent interactions within the laser-induced plume. The synthesized nanofibers bear a striking similarity to natural ECM material morphology, most notably to the dimensions and nanotopology of collagen fibrils.

5. Influence of synthesized nanostructures on cells

5.1 Introduction

As previously discussed, the goal of this project was to test the suitability of the two types of synthesized nanostructures for cell growth surfaces. To the best of our knowledge, this was the first study to investigate cell interactions on glass that has been nanostructured via laser ablation. Furthermore, aside from laser ablation, fabrication of both nanotips and 3D nanofibrous networks on glass by a single fabrication technique has not been documented. Compared to its competitor techniques, laser ablation generates nanofibers directly from bulk material that are highly networked and, as shall be discussed, display a higher order of nanotopology that is more representative of natural ECM proteins. The nanotips generated in this work were also the first recorded instance of this particular morphology of Na_2O. In addition to nanotips negatively affecting cell adhesion or hydrophobicity [4,31,34-36], research has shown that increasing the sodium oxide content in bioactive glass can reduce cell proliferation [54]. Thus it was hypothesized that the networked SiO_2 nanofiber structures would act as an aECM aiding in cell growth, while surfaces with Na_2O nanotip structures would be detrimental to cells.

For this proof-of-concept study, fibroblast-type cells were chosen due to the relative ease with which they can be cultured [14]. Fibroblasts are found in connective tissues of animals; they are typically responsible for secreting precursors of collagen and the other proteins that constitute the ECM. Frequently described as spindle-shaped (wide in the middle but tapering at both ends), fibroblasts in culture are large, flat, and elongated in appearance. However, in tissues, fibroblasts are likely to show more complexity, displaying cell processes (projections). When

tissues or organs suffer damage, fibroblasts migrate to the location of the trauma and aid in the repair process [14].

There are several notable structures of a cell (see Figure 5-1). The lamellipodia are the leading edge of a properly adhering motile cell [55]. Pseudopdia are cytoplasmic projections of a cell that help in their locomotion. Thin, filamentous varieties of pseudopodia are called filopodia and they act as antennae seeking nutrients and scouting directions for cell growth [56]. In fibroblasts especially, filopodia are used by the cell for migrating to and closing wounds [57]. The surface of a cell can also display thin, short projections called microvilli. These cellular extensions are important for cell motility and indicators of good cell attachment [58].

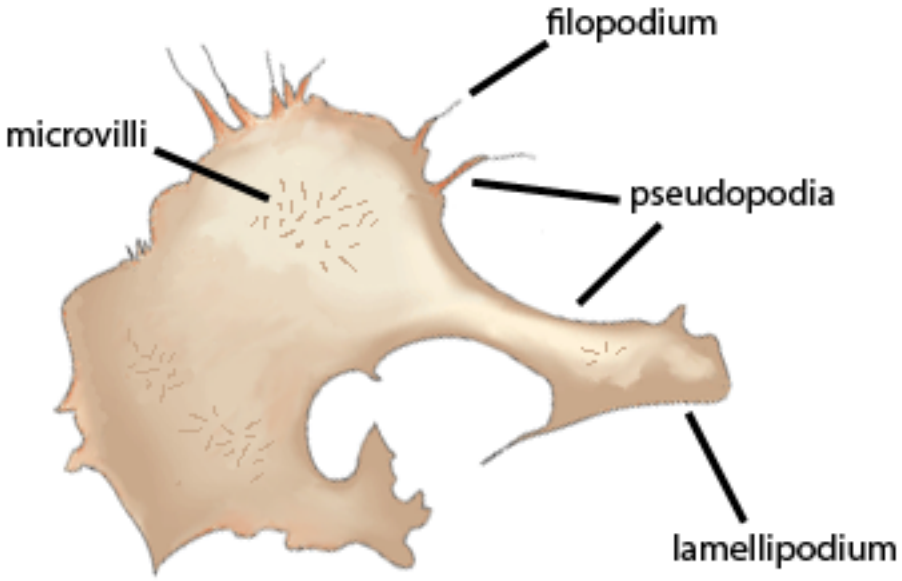

Figure 5-1 Diagram of a typical fibroblast and its notable structures, *Image modified from* [59].

Cells that have adhered to a surface but display none of the aforementioned structures are typically in the process of programmed cell death (apoptosis) [60]. Different from cellular death due to injury (necrosis), apoptosis is a mechanism that is begun after internal or external

biochemical signals are received by a cell. It is important to note that without apoptosis an organism would suffer from uncontrolled cell proliferation (i.e. cancer).

5.2 Nanotips

Fibroblasts were grown on bare glass slides with nanotips synthesized on the surface (see Figure 5-2). After a 24 hour incubation period, the cells were chemically fixed and examined under a SEM. Cells were not grown on the curved type nanotips synthesized on gold coated glass. The reasons for this were twofold. First, the morphology of both structures is exceedingly similar. Second, gold nanoparticles have been shown to interfere with cell proliferation [61] adding a further layer of complexity in interpreting potential results.

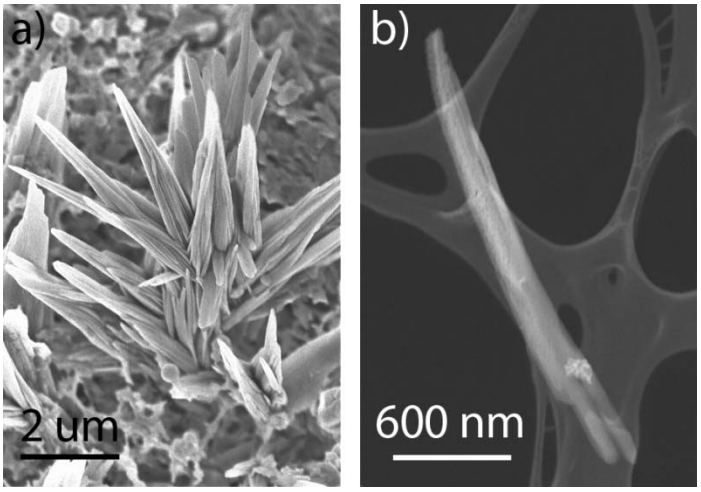

Figure 5-2 Representative **a)** SEM micrograph of synthesized nanotip cluster; and **b)** TEM micrograph of nanotip fragment

5.2.1 Morphology of cells and nanotips

It was clear upon inspection after incubation that all nanotips had dissolved; however, the ablated zone (where the nanotips were synthesized) showed very different cell behavior from the unablated zone (see Figure 5-3). Many cells grew on the unablated region displaying healthy characteristics such as lamellipodia and filopodia. In contrast, few cells were found on the

ablated region and those that did express were clearly in the process of apoptosis based on their shrunken, rounded shape.

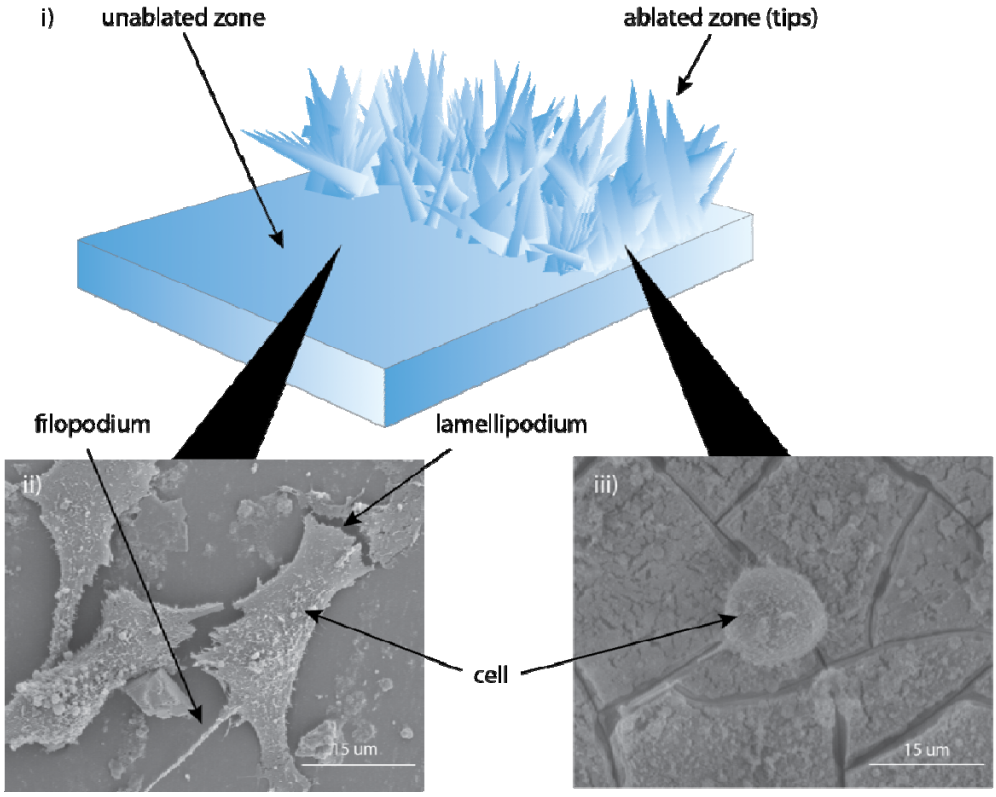

Figure 5-3 Diagram of **i)** nanotip structures synthesized on glass substrate; and corresponding SEM micrographs of fibroblasts that **ii)** grew well on unablated areas; and **iii)** were apoptotic on ablated areas.

5.3 Nanofibers

Nanofibrous surfaces synthesized on glass slides were used as cell growth substrates. Following incubation periods of 12 hrs, 1 day, or 1 week the cells were fixed and inspected using a SEM.

5.3.1 Morphology of cells and nanofibers

The cross-linking between the synthesized SiO_2 fibers is similar in organization to the binding protein fibronectin found in nearly all types of ECM structures. This same 3D network

model is also reflected in a type of collagen that is only present in a specific ECM structure known as the basement membrane (See Figure 5-4).

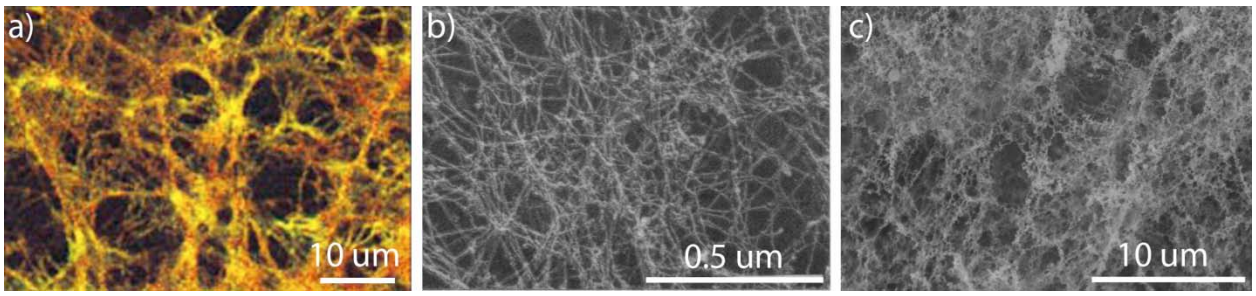

Figure 5-4 The networked matrix structures of **a)** fluorescently dyed fibronectin via confocal scanning; **b)** collagen in basement membrane via SEM micrograph; and **c)** synthetic SiO_2 nanofibers via SEM micrograph, *Images a) modified from* [62] *and b) from* [63].

Furthermore, the typical sub 100 nm diameter of SiO_2 nanoparticles agglomerate into nanofibers with equally small diameters. Such fibers are analogous in morphology to the collagen fibers found in non-basement membrane ECM tissues (See Figure 5-5). Not only are the synthesized nanofibers comparable in diameter to their natural counterparts, the repeating individual nanoparticles that constitute a synthetic nanofiber ensure a repeating pattern that is similar to the periodic band structure of collagen.

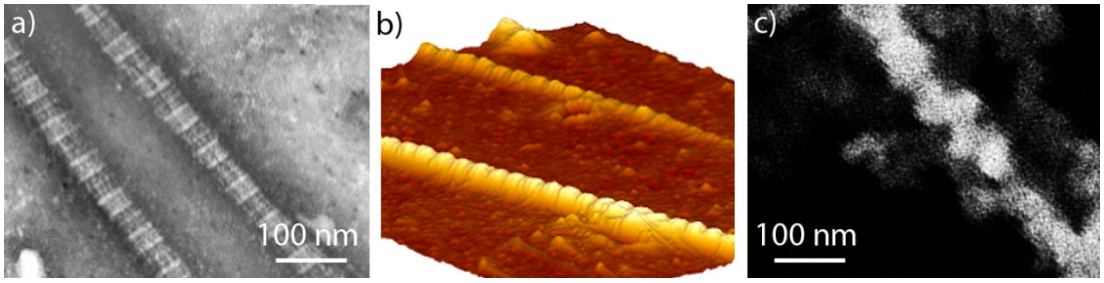

Figure 5-5 A morphological comparison of collagen by **a)** TEM micrograph; and **b)** Atomic Force Microscopy micrograph; to **c)** SEM micrograph of synthetic SiO_2 nanofibers, *Images a) and b) modified from* [64].

Imaging revealed that when nanofibers were immersed in cell media solution two types of structural degradation were instigated (see Figure 5-6). Some nanofibers would clump together losing their characteristic loop-like structures, while others would erode (presumably

detaching from the substrate or each other). Combinations of the two types of degradation were also observed. While the extent of degradation would vary within a single sample, it seemed to increase with incubation time. Cells that were introduced concurrently with the media grew on the nanofibrillar zones and displayed different traits from the cells growing in unprocessed regions. A breakdown by incubation period follows.

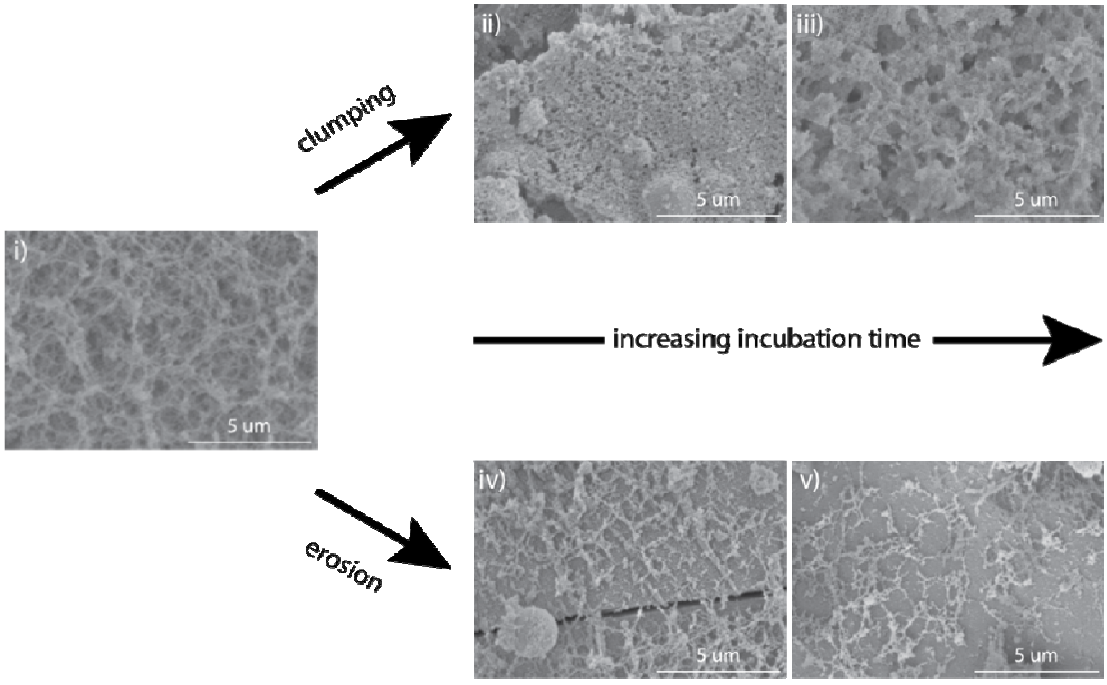

Figure 5-6 Representative SEM micrographs of **i)** typical nanofiber formations; and their degradation with time via **ii)**, **iii)** clumping; and **iv)**, **v)** erosion.

5.3.1.1 Incubation for 12 hours

Both types of nanofiber structural degradation were observed after 12 hours of incubation (see Figure 5-7). The inset in Figure 5-7ii shows fibers that have clumped together while insets in Figure 5-7iii show fibers that have clumped and eroded. The filopodia in Figure 5-7ii grew on top of the fibers and are morphologically similar to the cells that grew on unablated glass (Figure 5-7iv). However, the filopodia in Figure 5-7iii (see insets) appear to be adhering to the remnant fibers and not to the areas of bare glass. Furthermore, the pseudopodial surfaces of the fibroblasts that grew on unablated glass and on un-eroded fibers showed less texturing than the cells that

grew on eroded fibers. The average width and length of cells growing in the unablated region was 11 and 50 µm respectively. Cells that grew on the nanofibrous zone were typically smaller at 10 µm in width 30 µm in length.

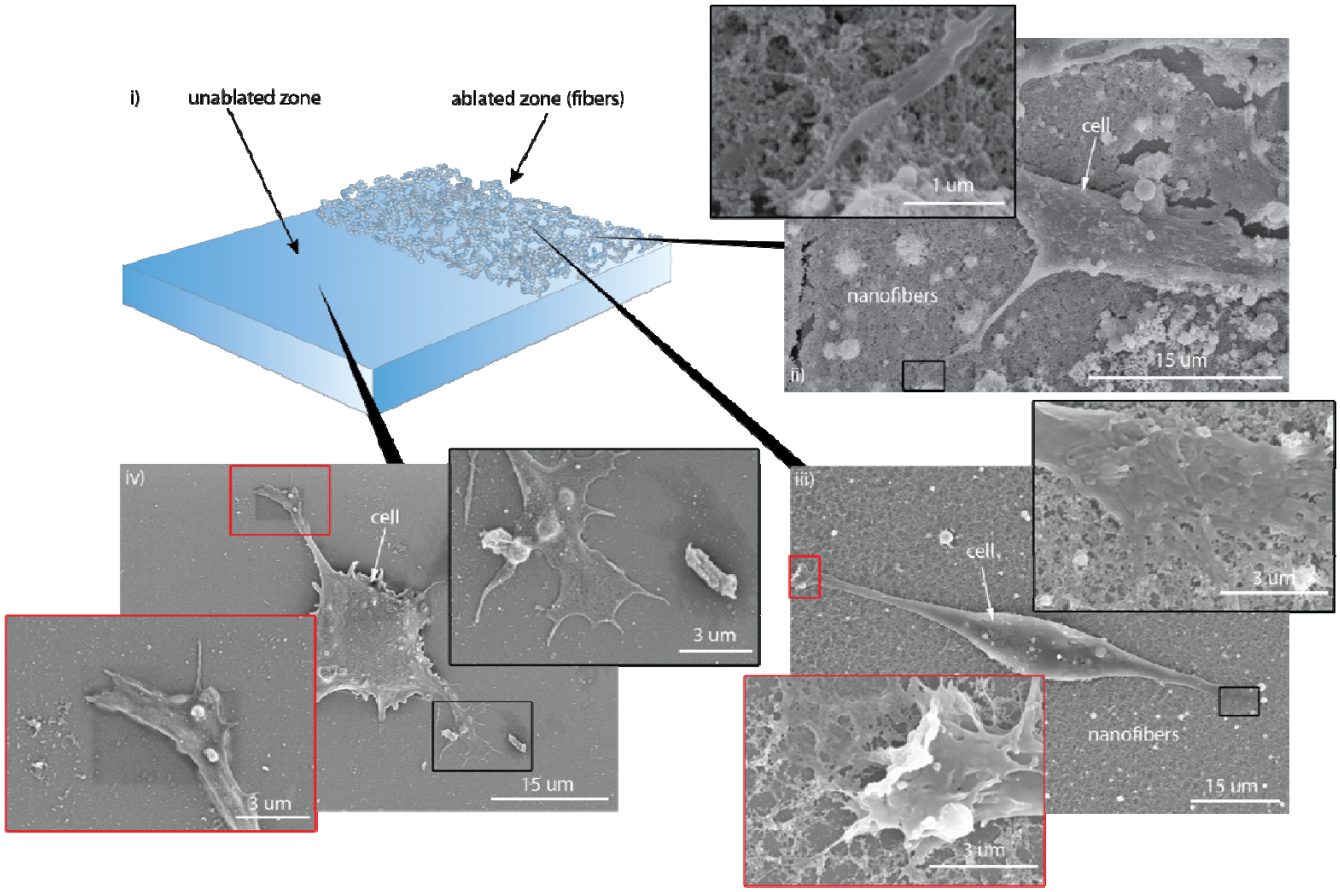

Figure 5-7 Diagram of **i)** nanofiber structures synthesized on glass substrate after 12 hr incubation; and corresponding SEM micrographs of fibroblasts that **ii)** grew on clumped nanofibers; **iii)** clumped and eroded nanofibers; and on **iv)** unablated areas. Insets are color coded magnifications of filopodia of the respective cells.

5.3.1.2 Incubation for one day

After a day of incubation much nanofiber erosion was evident as seen in the red and blue insets of Figure 5-8ii. These eroded fibers were once again, preferred adhesion sites for filopodial branches. Many filopodia were roughly the same size as the fibers themselves but recognizable by their length and relative straightness. The black inset of Figure 5-8ii is of a

region where there was relatively little fiber degradation. This mostly intact nanofibrous area was clearly an adhesion point for a pseudopodial leg of the fibroblast; however, almost no filopodia could be easily distinguished. The surface of the fibroblast lamellipodium in Figure 5-8ii appeared to be heavily textured. The cauliflower-like appearance seemed to be due to clumped nanofibers. A difference in morphology between cells that grew in the two zones was also apparent. Cells in the unablated zone (Figure 5-8iii) were wider while those in the ablated zone retained their thinner spindle shape.

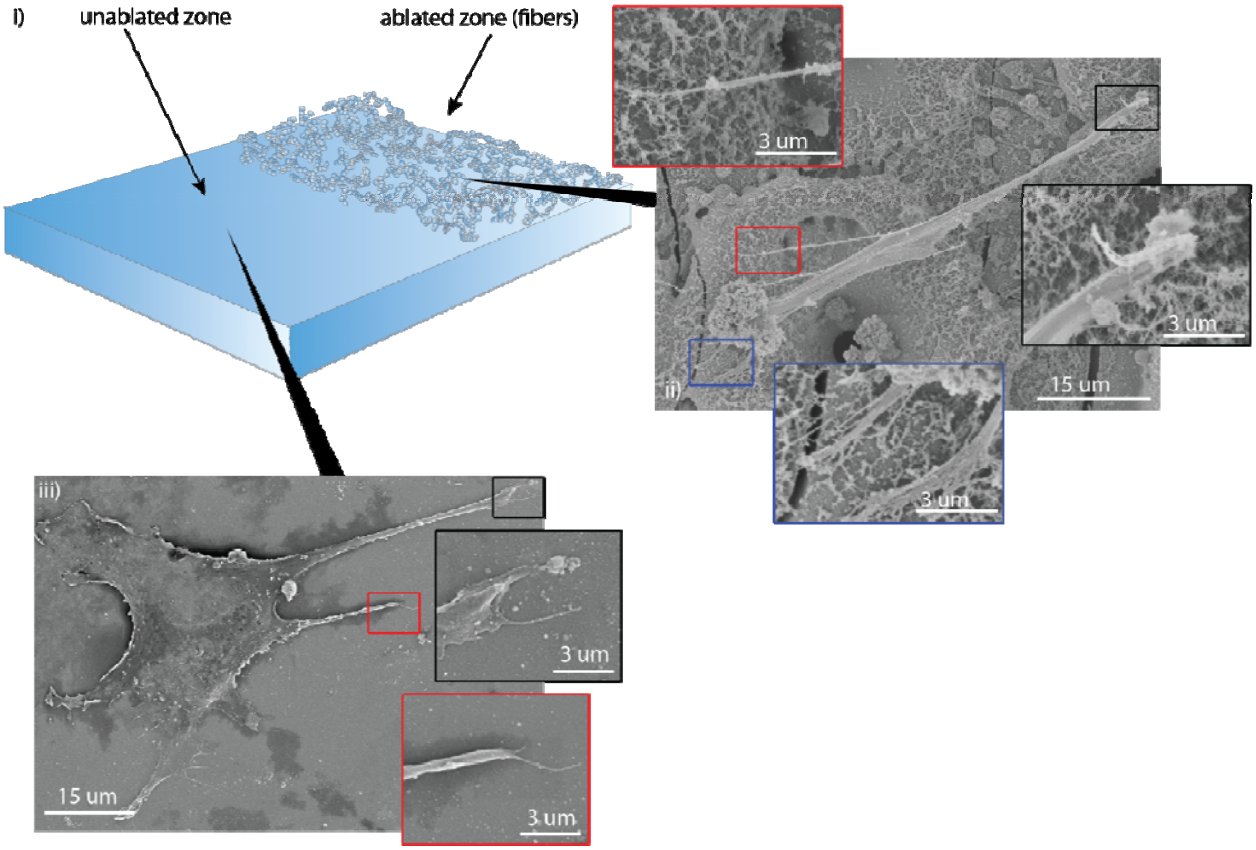

Figure 5-8 Diagram of **i)** nanofiber structures synthesized on glass substrate after 1 day incubation; and corresponding SEM micrographs of fibroblasts that **ii)** grew on eroded nanofibers; and on **iii)** unablated areas. Insets are color coded magnifications of filopodia of the respective cells.

5.3.1.3 Incubation for one week

Following a week of incubation the nanofibers appeared to have completely degraded. A well-defined boundary delineated by fibroblast growth could be seen between the laser processed and unprocessed regions (see Figure 5-9). The fibroblasts in the unablated zone grew into a confluent, randomly oriented monolayer while the fibroblasts on the laser ablated zone contained clusters of cells showing signs of organized, directional growth. These cell clusters (see Figure 5-9iv) were approximately 30 μm at their widest and over 100 μm long. Also visible in Figure 5-9iv are nanoscale cracks on the surface of the glass substrate. Individual cells were approximately equal in length regardless of their region of growth. However, fibroblasts in the ablated zone were consistently thinner (10 vs. 15 μm) than their unablated zone counterparts. Fibroblast surfaces in both regions also displayed microvilli, a feature unseen at the shorter incubation times. Closer inspection of the pseudopodial extensions of fibroblasts in both regions (Figure 5-9v and vi) reveal that cells that grew in the laser ablated zone have far more microvilli covering the surface. Also, due to the dissolution of fibers at this long incubation time, clear views of the glass substrate were available and it was apparent that nanoscale cracks existed on the glass surface.

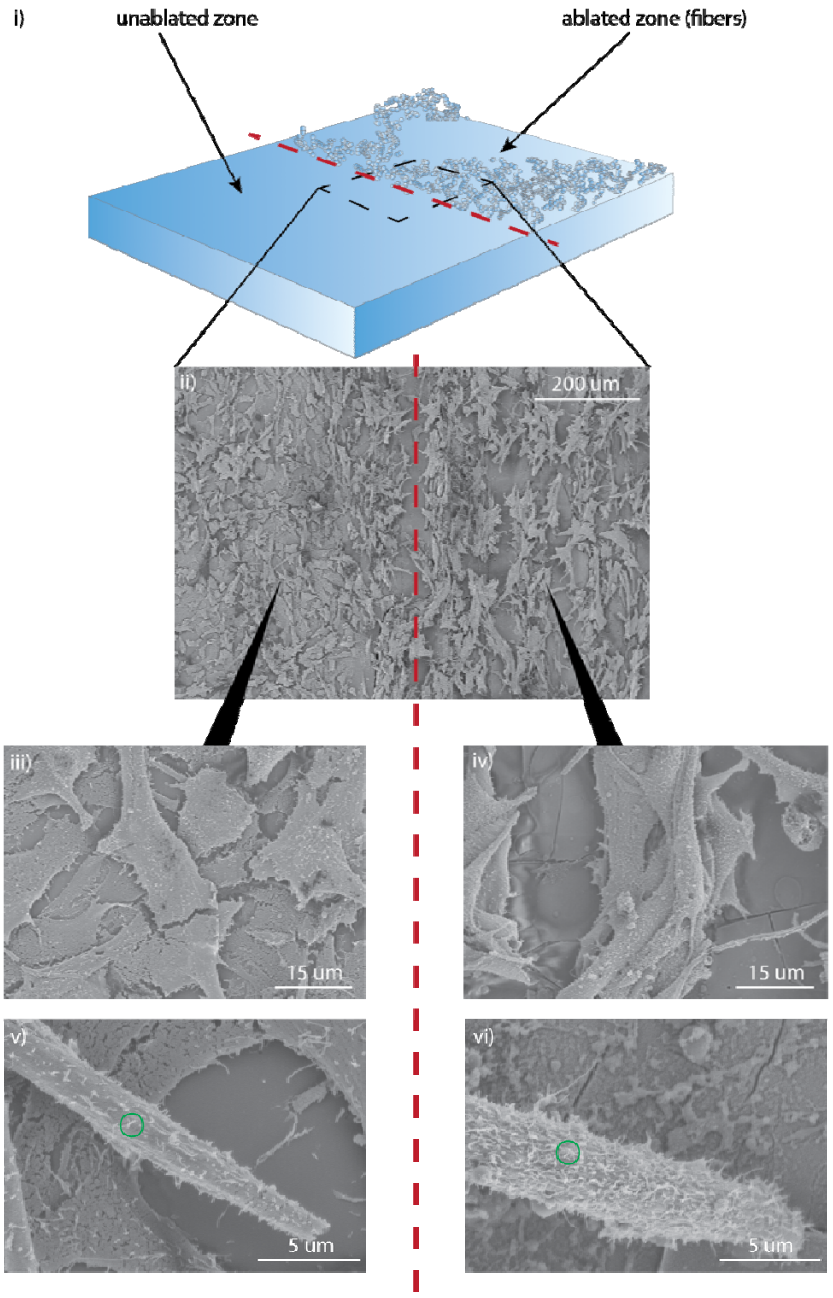

Figure 5-9 Diagram of **i)** nanofiber structures synthesized on glass substrate after 1 week incubation; and corresponding SEM micrographs of fibroblasts that **ii)** grew near the interface between ablated and unablated zones; and representative magnifications of cells in the **iii)** unablated and **iv)** ablated areas; and further magnifications of **v)**, **vi)** cell pseudopodia and microvilli (green circle) in each region.

5.4 Discussion

The two types of synthesized nanostructures showed very different results as cell growth substrates. The glass surfaces with nanotip structures induced cells to die, while the nanofiber structures provided good cell growth behavior that was unlike standard, unstructured, glass surfaces. These differences can likely be explained by considerations of nanostructure composition and morphology.

As shown here experimentally, the nanotips created on the soda-lime glass substrate were composed of sodium oxide. This result while previously unknown was nevertheless unsurprising since Na_2O is a major component of soda-lime silicates. Interestingly, studies have shown that increasing the sodium oxide content of glass can induce a cytotoxic response in cells [54]. Furthermore, nanorod and nanotip structures on surfaces have been shown to impair cell adhesion [4,31,34-36]. Complications with this explanation arise when consideration is given to the reactivity of Na_2O in aqueous media. While the nanotips may initially prevent cell adhesion, as the tips dissolve, their effectiveness would be compromised. Here, the sodium oxide may provide a clue as to the continued cytotoxic potential of the laser ablated surface. It can be assumed that after exposure to cell media, the Na_2O from the nanotips would be converted into sodium hydroxide (NaOH); however, sodium oxide that was brought to the surface as liquid melt via laser ablation and not subsequently turned into nanotips would remain near the surface. This reorganization due to melting and hardening might have the effect of locally increasing the sodium oxide content of the glass; hence, the reduction in cell adhesion even after nanotip dissolution.

The composition of the nanofibers was shown to be different from nanotips, with silicon dioxide nanoparticles agglomerating to form the nanofibrous network. It is known that SiO_2

nanoparticles are insoluble [65], but the clumping behavior in aqueous media observed here has previously been reported in commercial nanoparticle powders [66]. The eventual erosion of fibers with time has yet to be understood but as discussed earlier, implantable substrates for cell and tissue growth are greatly enhanced if the substrate material is both degradable and bioactive. Both meso and microporous silicon have displayed bioactivity in the past [67,68]. Therefore, given the increased reactivity inherent to materials with nano morphology, it may be expected that the nanofibrous silica structures described herein, will surpass larger silicon structures in bioactive measurements.

Further, while the nanoparticle constituents of the fibrous structure contribute to its degradation it also imparts a distinct advantage that is not seen in other nanofiber materials. Where other synthesis methods (e.g. electrospinning) yield fairly smooth fibers, the fibers reported here have increased nanotopology due to the individual nanoparticles that agglomerate. This results in more sites for cell adhesion to take place and could help explain the observed preference of cell filopodia to adhere to nanofibers rather than bare glass even after significant fiber degradation has taken place.

The ordered cell clusters that were observed at the one week interval are somewhat puzzling. Directionality in cell growth has previously been obtained by using micro/nano grooved surfaces or mats of unidirectional fibers [33,69,70]. The as fabricated fibers in this study are not unidirectional, moreover, the ~10 μm diameter microvia used in ablation are arranged in a grid pattern with a center-to-center spacing of 500 μm, a distance that is too far to create grooves. With the near complete degradation of fibers the ablated glass surface could be seen to display nanoscale cracks. It may be that without nanoscale fibers competing as adhesion points, the fibroblasts preferentially oriented along the cracks in the glass.

Although microvilli were not observed on the seeded fibroblasts until a week into incubation, the structures were apparent in much larger numbers on the pseudopodia of fibroblasts in the ablated areas. This could insinuate a higher quality of fibroblast attachment within the ablated zone.

5.5 Summary

Both nanotip and nanofiber structures degraded in the process of seeding the substrates with fibroblasts. Nanotips were not present after 24 hours of cell incubation whilst nanofibers took significantly longer to degrade. Fibroblasts on the nanotip surfaces showed signs of apoptosis but cells on the nanofiber surfaces expressed healthily. The cellular structure responsible for securing the fibroblast to a suitable scaffold preferentially adhered to nanofibers rather than to bare glass in the ablated zone. This was observed even after significant fiber degradation. Aligned clusters of cells that were seen after a week of incubation may be due to orientation along nanoscale cracks in the glass that provided alternative adhesion points for fibroblasts after the dissolution of nanofibers. After a week of incubation higher numbers of microvilli on the surface of cells in the ablated zone were observed and may be an indicator of better adhesion.

6. Conclusion and Future Work

6.1 Conclusion

Using the ultrafast laser ablation technique, two types of nanostructured surfaces, nanotips and nanofibers, have been created on easily accessible, standard, microscope slide glass substrates. The raw materials used to produce these nanostructures originate from the substrate itself and the process does not require the use of additional wet chemicals or catalysts. Furthermore, the nanostructures are created in an ambient environment. These unique features are not found in most other synthesis methods and result in a simplified procedure for developing nanomaterials with a low risk of chemical contamination.

Control over the width of generated nanotips via laser dwell time has been demonstrated, with longer times resulting in denser clusters of thinner nanotips. The composition and morphology of the nanotips and nanofibers has been investigated. The nanotips are shown to be primarily sodium oxide and a new structure formation mechanism has been proposed. The process begins with the melting of the glass substrate and separation by molecular density. This is quickly followed by melt ejection of polar Na_2O particles that interact electrostatically with laser ionized nitrogen creating the characteristic nanotip shape. The 3D networked, nanofibers are shown to form from agglomerated silicon dioxide nanoparticles that are likely produced by the well-known vapor condensation method in laser ablation.

Initial characterization of the biomedical potential of the synthesized nanostructures has been completed. Apoptotic cell behavior of NIH 3T3 embryonic mouse fibroblasts is observed on nanotip surfaces. This indicates that the nanotip surfaces generated in this work might be used in antibacterial or contra-cell applications. Conversely, the surface of intensely interconnected

nanofibers has been shown to mimic natural ECM morphology and act as suitable scaffolds for cell growth. Furthermore, the laser synthesized nanofibers showed a nanotopology not present in other aECM materials closely mimicking the repeating structure of certain collagen fibers. Inspection of fibroblast substrate interactions reveal that filopodia in the ablated zone prefer to adhere to nanofibers rather than bare glass, even as the fibers degrade over time. Furthermore, at long incubation time fibroblasts growing in the ablated zone display higher numbers of microvilli on their surface, this could suggest a higher quality of cell adhesion.

By choosing when to use nitrogen flow over the ablation site it would be trivial to generate both nanotips and nanofibers that were localized to specific regions of a single glass substrate. Such selective treatment could be used to create a type of surface with both growth-positive and growth-negative zones for cells. This could lead to the development of a new class of surface treatments for use as biological testing equipment.

6.2 Next steps

While a successful proof-of-concept aECM has been fabricated, further characterization of the SiO_2 nanofibers and their cellular interactions is required. Specific suggestions include biological assays that can provide quantitative measurements of cell adhesivity and biocompatibility. Furthermore, targeted fluorescent dyes could be employed to stain specific receptors in cells, and combined with fluorescence microscopy, a deeper understanding of cell behavior on nanofiber substrates might be gleaned. In this work, only fibroblasts were seeded on the substrates but other cell types could display very different growth behavior. In particular, osteoblasts (bone forming cells) and bioactive glasses are known to interact extremely well.

Modifications to the synthesized nanofibers are another possible avenue of exploration. A current protocol for enhancing cell attachment to standard cell culturing surfaces (e.g. petri

dishes) is to coat them with ECM proteins such as fibronectin and allowing to air dry before seeding cells. The same technique could be replicated on the nanofibrous substrates described in this work. The porous nature of the scaffold also provides space for incorporating therapeutic macromolecules (i.e. medication). However, in functionalizing the substrates, care would have to be taken not to compromise the nanomorphology of the fibers.

References

[1] Feynman RP: **There's plenty of room at the bottom.** J Microelectromech S 1992, **1**(1):60-66. Print Rpt. of "There's plenty of room at the bottom". California Institute of Technology, Annual Meeting American Physical Society. Pasadena, California. 26 Dec 1959.

[2] Taniguchi N: **On the Basic Concept of 'Nano-Technology'.** Proc. Intl. Conf. Prod. Eng., Tokyo, Part II, Japan Society of Precision Engineering, 1974, pp 18-23.

[3] Breuer O, Sundararaj U: **Big Returns From Small Fibers: A Review of Polymer/Carbon Nanotube Composites.** Polym Composite 2004, **25**(6): 630-645.

[4] Park K-C, Choi HJ, Chang C-H, Cohen RE, McKinley GH, Barbastathis G: **Nanotextured Silica Surfaces with Robust Superhydrophobicity and Omnidirectional Broadband Supertransmissivity.** ACS Nano 2012, **6**(5):3789-3799.

[5] Armstrong RX, Baschung B, Booth DW, Samirant M: **Enhanced Propellant Combustion with Nanoparticles.** Nano Lett 2003, **3**(2):253-255.

[6] Lin YS, Wei CT, Olevsky EA, Meyers MA: **Mechanical properties and the laminate structure of Arapaima gigas scales.** J Mech Behav Biomed 2011, **4**(7):1145-1156.

[7] Jakubinek MB, Samarasekera CJ, White MA: **Elephant ivory: A low thermal conductivity, high strength nanocomposite.** J Mater Res 2006, **21**(1):287-292.

[8] Mandelkern M, Elias JG, Eden D, Crothers DM: **The Dimensions of DNA in Solution.** J Mol Biol 1981, **152**(1):153-161.

[9] Erickson HP: **Size and Shape of Protein Molecules at the Nanometer Level Determined by Sedimentation, Gel Filtration, and Electron Microscopy.** Biol Proced Online 2009, **11**(1):32-51.

[10]Williams DF: **On the mechanisms of biocompatibility.** Biomaterials 2008, **29**(20):2941-2953.

[11] Williams DF (Ed): *Definitions in Biomaterials*. Amsterdam: Elsevier, 1987.

[12] Hench LL, Paschall HA: **Direct chemical bond of bioactive glass-ceramic materials to bone and muscle.** J Biomed Mater Res 1973, **7**(3):25-42.

[13] Hench LL: **Bioceramics.** J Am Ceram Soc 1998, **81**(7):1705-1727.

[14] Alberts B, Johnson A, Lewis J, Raff M, Roberts K, Walter P: *Molecular Biology of the Cell*. New York: Garland Science; 2008.

[15] Pesciotta Peters DM, Chen Y, Zardi L, Brummel S: **Conformation of Fibronectin Fibrils Varies: Discrete Globular Domains of Type III Repeats Detected.** Microsc Microanal 1998, **4**(4):385-396.

[16] Curtis A, Wilkinson C: **Topographic control of cells.** Biomaterials 1997, **18**(24):1573-1583.

[17] Hynes RO: **The Extracellular Matrix: Not Just Pretty Fibrils.** Science 2009, **326**(5957):1216-1219.

[18] Lin J, Wang X, Ding B, Yu J, Sun G, Wang M: **Biomimicry via Electrospinning.** Crit Rev Solid State 2012, **37**(2):94-114.

[19] Li D, Xia Y: **Electrospinning of Nanofibers: Reinventing the Wheel?.** Adv Mater 2004, **16**(14):1151-1170.

[20] Lin JY, Ding B, Yu JY, Hsieh Y: **Direct Fabrication of Highly Nanoporous Polystyrene Fibers via Electrospinning.** ACS Appl Mater Interfaces 2010, **2**(2):521-528.

[21] Larsen G, Velarde-Ortiz R, Minchow K, Barrero A, Loscertales IG: **A Method for Making Inorganic and Hybrid (Organic/Inorganic) Fibers and vesicles with Diameters in the Submicrometer and Micrometer Range via Sol-Gel Chemistry and Electrically Forced Liquid Jets.** J Am Chem Soc 2003, **125**(5):1154-1155.

[22] Kim H-W, Kim H-E, Knowles JC: **Production and Potential of Bioactive Glass Nanofibers as a Next-Generation Biomaterial.** Adv Funct Mater 2006, **16**(12):1529-1535.

[23] Praeger M, Saleh E, Vaughan A, Stewart WJ, Loh WH: **Fabrication of nanoscale glass fibers by electrospinning.** Appl Phys Lett 2012, **100**(6):063114, 10 pages, doi:10.1063/1.3684940.

[24] Quintero F, Pou J, Lusquiños F, Boutinguiza M, Soto R, Pérez-Amor M: **Large-scale fast production of amorphous Si-Al-O nanowires under ambient conditions.** Appl Phys A: Mater Sci Process 2004, **78**(3):295-298.

[25] Quintero F, Mann AB, Pou J, Lusquiños F, Riveiro A: **Rapid production of ultralong amorphous ceramic nanofibers by laser spinning.** Appl Phys Lett 2007, **90**(15):153109, 3 pages, doi:10.1063/1.2722202.

[26] Quintero F, Pou J, Comesaña R, Lusquiños F, Riveiro A, Mann AB, Hill RG, Wu ZY, Jones JR: **Laser Spinning of Bioactive Glass Nanofibers.** Adv Funct Mater 2009, **19**(19):3084-3090.

[27] Whitesides GM, Grzybowski B: **Self-Assembly at All Scales.** Science 2002, **295**(5564):2418-2421.

[28] Hartgerink JD, Beniash E, Stupp SI: **Self-Assembly and Mineralization of Peptide-Amphiphile Nanofibers.** Science 2001, **294**(5547):1684-1688.

[29] Ma PX, Zhang R: **Synthetic nano-scale fibrous extracellular matrix.** J Biomed Mater Res 1999, **46**(1):60-72.

[30] Yang F, Murugan R, Ramakrishna S, Wang X, Ma Y-X, Wang S: **Fabrication of nano-structured porous PLLA scaffold intended for nerve tissue engineering.** Biomaterials 2004, **25**(10):1891-1900.

[31] Lee J, Kang BS, Hicks B, Chancellor TF, Chu BH, Wang H-T, Keselowsky BG, Ren F, Lele TP: **The control of cell adhesion and viability by zinc oxide nanorods.** Biomaterials 2008, **29**(27):3743-3749.

[32] Suh CW, Kim MY, Choo JB, Kim JK, Kim HK, Lee EK: **Analysis of protein adsorption characteristics to nano-pore silica particles by using confocal laser scanning microscopy.** J Biotechnol 2004, **112**(3):267-277.

[33] Chen J, Ulerich JP, Abelev E, Fasasi A, Arnold CB, Soboyejo WO: **An investigation of the initial attachment and orientation of osteoblast-like cells on laser grooved Ti-6Al-4V surfaces.** Mater Sci Eng, C 2009, **29**(4):1442-1452.

[34] Lee J, Chu BH, Sen S, Gupte A, Chancellor TJ, Chang C-Y: **Modulating malignant epithelial tumor cell adhesion, migration and mechanics with nanorod surfaces.** Biomed Microdevices 2011, **13**(1):89-95.

[35] Ranella A, Barberoglou M, Bakogianni S, Fotakis C, Stratakis E: **Tuning cell adhesion by controlling the roughness and wettability of 3D micro/nano silicon structures.** 2010, **6**(7):2711-2720.

[36] Hong C-C, Huang P, Shieh J: **Fabrication of Morphology-Controlled Sub-20-nm Polymer Nanotip and Nanopore Arrays Using an Identical Nanograss Mold.** Macromolecules 2010, **43**(18):7722-7728.

[37] Wang Y, Du G, Liu H, Liu D, Qin S, Wang N, Hu C, Tao X, Jiao J, Wang J, Wang ZL: **Nanostructured Sheets of Ti-O Nanobelts for Gas Sensing and Antibacterial Applications.** Adv Funct Mater 2008, **18**(7):1131-1137.

[38] Gao B, Fu J, Huo K, Zhang W, Xie Y, Chu PK: **Quasi-Aligned Ag-Nb_2O_5 Nanobelt Arrays with Enhanced Photocatalytic and Antibacterial Activities.** J Am Ceram Soc 2011, **94**(8):2330-2338.

[39] Tan B, Venkatakrisnan K: **Synthesis of fibrous nanoparticle aggregates by femtosecond laser ablation in air.** Opt Express 2009, **17**(2):1064-1069.

[40] Sivakumar M, Venkatakrishnan K, Tan B: **Synthesis of Nanoscale Tips Using Femtosecond Laser Radiation under Ambient Condition.** Nanoscale Res Lett 2010, **5**(2):438-441.

[41] Pedrotti FL, Pedrotti LS: *Introduction to Optics*. New Jersey: Prentice Hall; 1993.

[42] Gamaly EG: **The physics of ultra-short laser interaction with solids at non-relativistic intensities.** Phys Rep 2011, **508**(4-5):91-243.

[43] Luther-Davies B, Rode AV, Madsen NR, Gamaly EG: **Picosecond high-repetition-rate pulsed laser ablation of dielectrics: The effect of energy accumulation between pulses.** Opt Eng 2005, **44**(5):1-8.

[44] Gattass RR, Mazur E: **Femtosecond laser micromachining in transparent materials.** Nature Photon 2008, **2(**4):219-225.

[45] Lushinkov AA: **Laser Induced Aerosols.** J Aerosol Sci 1996, **27**(Suppl. 1):S377-S378.

[46] Webb RL, Dickinson JT, Exarhos GJ: **Characterization of Particulates Accompanying Laser Ablation of $NaNO_3$.** Appl Spectrosc 1997, **51**(5):707-717.

[47] Yoo JH, Jeong SH, Grief R, Russo RE: **Explosive change in crater properties during high powered nanosecond laser ablation of silicon.** J Appl Phys 2000, **88**(3):1638-1649.

[48] Harilal SS, Bindhu CV, Tillack MS, Najmabadi F, Gaeris AC: **Internal structure and expansion dynamics of laser ablation plumes into ambient gases.** J Appl Phys 2003, **93**(5):2380-2388.

[49] Sasaki K, Watarai H: **Reaction between laser ablation plume and ambient gas studied by laser-induced fluorescence imaging spectroscopy.** JPCS 2007, **59**(1):60-63.

[50] Venkatakrishnan K, Vipparty D, Tan B: **Nanofibre fabrication by femtosecond laser ablation of silica glass.** Opt Express 2011, **19**(17):15770-15776.

[51] Couairon A, Mysyrowicz A: **Femtosecond Filamentation in Air.** In: *Progress in Ultrafast Intense Laser Science Volume I*. Edited by: Yamanouchi K, Chin SL, Agostini P, Ferrante G. Heidelberg: Springer Berlin; 2006:235-258.

[52] Sivakumar M, Venkatakrishnan K, Tan B: **Synthesis of Glass Nanofibers Using Femtosecond Laser Radiation Under Ambient Condition.** Nanoscale Res Lett 2009, **4**(11):1263-1266.

[53] Sun J, Longtin JP: **Inert gas beam delivery for ultrafast laser micromachining at ambient pressure.** J Appl Phys 2001, **89**(12):8219-8224.

[54] Wallace KE, Hill RG, Pembroke JT, Brown CJ, Hatton PV: **Influence of sodium oxide content on bioactive glass properties.** J Mater Sci: Mater Med 1999, **10**(12):697-701.

[55] Small JV, Stradal T, Vignal E, Rottner K: **The lamellipodium: Where motility begins.** Trends Cell Biol 2002, **12**(3):112-120.

[56] Mattila PK, Lappalainen P: **Filopodia: molecular architecture and cellular functions.** Nat Rev Mol Cell Bio 2008, **9**(6):446-454.

[57] Mellor H: **The role of formins in filopodia formation.** Biochim Biophys Acta 2010, **1803**(2):191-200.

[58] Al-Hiyasat AS, Al-Sa'eed OR, Darmani H: **Quality of cellular attachment to various root-end filling materials.** J Appl Oral Sci 2012, **20**(1):82-88.

[59] Luo L: **RHO GTPases in neuronal morphogenesis.** Nat Rev Neurosci 2000, **1**(3):173-180.

[60] Häcker Georg: **The morphology of apoptosis.** Cell Tissue Res 2000, **301**(1):5-17.

[61] Pan Y, Bartneck M, Jahen-Dechent W: **Cytotoxicity of gold nanoparticles.** Method Enzymol 2012, **509**:225-242.

[62] Raghunnath M, Tschödrich-Rotter M, Sasaki T, Meuli M, Chu M-L, Timpl R: **Confocal Laser Scanning Analysis of the Association of Fibulin-2 with Fibrillin-1 and Fibronectin Define Different Stages of Skin Regeneration.** J Invest Dermatol 1999, **112**(1):97-101.

[63] Yurchenco PD, Ruben GC: **Basement Membrane Structure In Situ: Evidence for Lateral Associations in the Type IV Collagen Network.** J Cell Biol 1987, **105**(6 I):2559-2568.

[64] Bayer ML, Yeung C-YC, Kadler KE, Qvortrup K, Baar K, Svensson RB, Magnusson SP, Krogsgaard M, Koch M, Kjaer M: **The initiation of embryonic-like collagen fibrillogenesis by adult human tendon fibroblasts when cultured under tension.** Biomaterials 2010, **31**(18):4889-4897.

[65] Perry RH, Green DW: *Perry's Chemical Engineers' Handbook*. New York: McGraw-Hill; 2007.

[66] Tso C-P, Zhung C-M, Shih Y-H, Tseng Y-M, Wu S-C, Doong R-A: **Stability of metal oxide nanoparticles in aqueous solutions.** Water Sci Technol 2010, **61**(1):127-133.

[67] Coffer JL, Whitehead MA, Nagesha DK, Mukherjee P, Akkaraju G, Totolici M, Saffie RS, Canham LT: **Porous silicon-based scaffolds for tissue engineering and other biomedical applications.** Phys Status Solidi A 2005, **202**(8):1451-1455.

[68] Canham LT: **Bioactive Silicon Structure Fabrication Through Nanoetching Techniques.** Adv Mater 1995, **7**(12):1033-1037.

[69] Bettinger CJ, Zhang Z, Gerecht S, Borenstein JT, Langer R: **Enhancement of In Vitro Capillary Tube Formation by Substrate Nanotopography.** Adv Mater 2008, **20**(1):99-103.

[70] Fu X, Wang H: **Spatial Arrangement of Polycaprolactone/Collagen Nanofiber Scaffolds Regulates the Wound Healing Related Behaviors of Human Adipose Stromal Cells.** Tissue Eng Part A 2012, **18**(5-6):631-642.

Glossary

aECM	A synthetic surface with structures organized to mimic the natural ECM.
Apoptosis	A process controlled by a diverse range of cell signals that programs a cell to die.
Cell	The smallest unit of life that is considered to be alive.
Collagen	A protein found in the ECM providing protection against tearing.
ECM	A naturally occurring, elaborately networked, fibrillar structure that gives shape to tissues and acts as a scaffold upon which cells may grow.
Elastin	A protein found in the ECM providing elasticity to the structure.
Fibroblast	A type of cell found in connective tissue, and involved in wound healing, that can secrete the proteins that form an ECM.
Fibronectin	A protein found in the ECM that helps to bind cells to the structure.
Filopodia	A thin filamentous variety of pseudopodia that extend past the lamellipodia of cells and help cells adhere to a surface.
Lamellipodia	The leading edge of a cell responsible for propelling mobile cells along surfaces.
Laminin	A protein found in the ECM that helps to bind cells to the structure.
Microvilli	Small protrusions on membranes of cells involved in adhesion to surfaces.
Pseudopodia	Temporary cell projections with varying morphology.